Doctoral Dissertation

Studies on the Defect-Mediated Electron Transfer in Photocatalysts

XUE JIAWEI

July 2020

Division of Applied Chemistry,
Graduate School of Engineering,
Osaka University

Preface

The studies presented in this thesis were carried out under the direction of Professor Mamoru Fujitsuka and Professor Tetsuro Majima, The Institute of Scientific and Industrial Research (SANKEN), Osaka University from October 2017 to September 2020.

The subject of this thesis is the understanding of the defect-mediated electron transfer in photocatalysts. The aim of this research is to unravel the role of defects in the photogenerated electron transfer in photocatalysts by combining experiments and theoretical simulations.

The author hopes that the results and conclusions presented in this thesis would guide the design and optimization of electron transfer reactions with high efficiency for photocatalysis.

XUE JIAWEI

Department of Applied Chemistry
Graduate School of Engineering
Osaka University
July 2020

Contents

General Introduction

Utilizing solar energy to drive catalytic reactions over semiconductor photocatalysts promises a green and sustainable energy society.[1] In a general picture, typical photocatalytic reactions consist of three processes (Figure 1): (i) photoexcitation of the semiconductor to generate charges (electrons and holes), (ii) charge separation (CS) and transfer, and (iii) surface catalytic reactions such as H_2 and O_2 evolution from water,[1] pollutant degradation,[2] CO_2 reduction,[3] N_2 fixation[4] and so on. Currently, the practical application of photocatalysis is still thwarted by the low conversion efficiency due to fast charge recombination and insufficient amount of reaction sites in photocatalysts.[5] Integrating a second component with abundant active sites to form a heterojunction architecture has been proved to be one of the most promising ways for resolving these problems because charges can be separated spatially due to the mismatch of the electronic band levels of each component.[6] With this development, the charge transfer process becomes more complicated, because charges are generated on different components, and generally transfer from one component to the other. Despite this, there remains the need to investigate the charge transfer process since it is the prerequisite to display the efficacy of the final catalytic reactions. Understanding such a process will guide the design and engineering of new photocatalysts for highly efficient catalytic reactions.

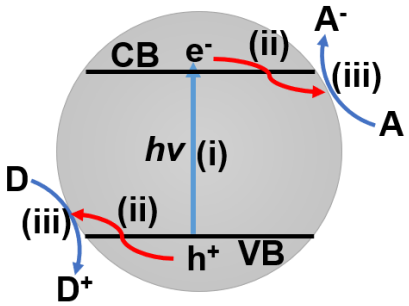

Figure 1. A schematic illustration of typical photocatalytic processes over a semiconductor photocatalyst. e^-, electron; h^+, hole; CB, conduction band; VB, valence band; A, acceptor; D, donor.

Another great hurdle for the application of photocatalysis is the poor light absorption ability of the photocatalysts. For example, traditional photocatalyst, TiO_2 can only absorb UV light ($\lambda < 400$ nm) which only accounts for less than 5% of the solar light energy, leaving visible light ($400 < \lambda < 780$ nm, ~43%) and near-infrared light ($780 < \lambda < 2500$ nm, ~52%) unutilized.[7] Over the past decades, many efforts have been made to extend the light absorption of photocatalysts. Among various strategies, defect engineering has great promise.[8] Defects extend the light absorption of semiconductors by regulating and modifying the electronic structures of semiconductors to add extra electronic transition pathways. To be specific, electronic transitions from the valence band (VB) to the defect states (DSs) and those from the DSs to the conduction band (CB) account for the extended light absorption (Figure 2a).[9] Defects are the places where the perfect arrangement of atoms is destroyed or broken, which intrinsically exist in semiconductors, especially in nanosized ones.[4] Figure 2b shows one of the most popular defects called as vacancy defect, where one atom is missing.

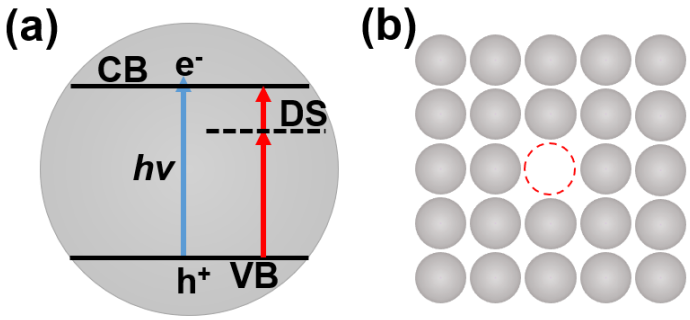

Figure 2. Schematic illustrations of (a) the electronic transitions mediated by the DSs and (b) one vacancy defect: the loss of one atom.

Currently, the effects of defects on the photocatalytic activity are still under debate. It has long been accepted that defects are detrimental to the photocatalytic activity because DSs are usually localized in the forbidden band of semiconductors, which makes the photogenerated charges immobile.[10–12] However, the positive effects of defects are gradually recognized, that is, defects can capture photogenerated electrons or holes to inhibit recombination.[13–15] Of note, such debates could be primarily resulted from the complex charge transfer processes mediated by defects. The unclear role of defects in the charge transfer has become a great hurdle for developing high-

performance photocatalysts by defect engineering.

From this viewpoint, in this dissertation, attention is focused on two typical photocatalytic reactions, H_2 evolution and pollutant degradation, where electrons play an important role. The defect-mediated photogenerated electron transfer (ET) in a series of typical photocatalysts is studied by a combination of experiments and theoretical simulations. As a result, the photocatalytic mechanisms are unraveled to guide the development of new and efficient photocatalysts.

Content of each chapter is described as below.

In Chapter 1, Au/TiO_2 mesocrystal (TMC) as a plasmonic photocatalyst prototype is investigated by using single-particle photoluminescence (PL) spectroscopy combined with finite-difference time-domain (FDTD) simulations. It is found that introduction of DSs builds up a channel for hot electrons with energies lower than the Schottky barrier height to transfer to the semiconductor, resulting in an enhanced photocatalytic degradation rate of methylene blue (MB).

In Chapter 2, the photocatalytic mechanism of the N-deficient carbon nitride (DCN) with N vacancies (V_ns) and cyano groups is studied by a combination of experimental investigations and density functional theory (DFT) calculations. It is found that the photocatalytic activity of DCN for H_2 evolution is restricted by the low mobility of the photogenerated electrons caused by defects, especially the cyano groups.

In Chapter 3, by taking carbon nitride (CN)/MoS_2 (MS) as a heterojunction photocatalyst prototype, it is unraveled that vacancies play a critical role in the interfacial ET (IET) of heterojunction photocatalysts. DFT calculations, combined with femtosecond time-resolved diffuse reflectance spectroscopy (fs-TDRS), give a clear picture that V_n states act as shallow trap states (STSs) for photogenerated electrons and thereby facilitate the IET process due to a large energy difference between STSs and CS states. Moreover, the excess electrons left by the loss of N atoms (producing V_ns) could partially transfer to MS to generate STSs in the forbidden band of MS, where the transferred photogenerated electrons could be further trapped to efficiently drive H_2 evolution.

In Chapter 4, the IET kinetics of CN/Pt as a semiconductor/cocatalyst prototype is investigated by fs-TDRS. It is found that the near bandgap excitation of CN inhibits the IET of CN/Pt due to electron deep trapping induced by intrinsic defects, resulting in a markedly decreased apparent quantum efficiency (AQE) for photocatalytic H_2 evolution.

In Chapter 5, the photogenerated electron kinetics of a thermal-decomposed CN (TCN) is investigated by fs-TDRS. It is found that the oxygen functional group (OFG) defects in TCN contribute to the formation of reactive STSs for photogenerated electrons, leading to an enhanced activity for photocatalytic H_2 evolution.

References

1. Q. Wang and K. Domen, *Chem. Rev.*, **2020**, 120, 919–985.
2. D. Chatterjee and S. Dasgupta, *J. Photochem. Photobiol. C*, **2005**, 6, 186–205.
3. J. L. White, M. F. Baruch, J. E. Pander, III, Y. Hu, I. C. Fortmeyer, J. E. Park, T. Zhang, K. Liao, J. Gu, Y. Yan, T. W. Shaw, E. Abelev and A. B. Bocarsly, *Chem. Rev.*, **2015**, 115, 12888–12935.
4. R. Shi, Y. Zhao, G. I. N. Waterhouse, S. Zhang and T. Zhang, *ACS Catal.*, **2019**, 9, 9739−9750.
5. W. Bi, L. Zhang, Z. Sun, X. Li, T. Jin, X. Wu, Q. Zhang, Y. Luo, C. Wu and Y. Xie, *ACS Catal.*, **2016**, 6, 4253−4257.
6. X. An, T. Li, B. Wen, J. Tang, Z. Hu, L.-M. Liu, J. Qu, C. P. Huang and H. Liu, *Adv. Energy Mater.*, **2016**, 6, 1502268.
7. S. Bai, J. Jiang, Q. Zhang and Y. Xiong, *Chem. Soc. Rev.*, **2015**, 44, 2893−2939.
8. S. Bai, N. Zhang, C. Gao and Y. Xiong, *Nano Energy*, **2018**, 53, 296−336.
9. A. Naldoni, M. Allieta, S. Santangelo, M. Marelli, F. Fabbri, S. Cappelli, C. L. Bianchi, R. Psaro and V. D. Santo, *J. Am. Chem. Soc.*, **2012**, 134, 7600–7603.
10. D. C. Cronemeyer, *Phys. Rev.*, **1959**, 113, 1222–1226.
11. S. K. Cushing, F. Meng, J. Zhang, B. Ding, C. K. Chen, C. Chen, R. Liu, A. D. Bristow, J. Bright, P. Zheng and N. Wu, *ACS Catal.*, **2017**, 7, 1742–1748.

12. M. Sachs, J.-S. Park, E. Pastor, A. Kafizas, A. A. Wilson, L. Francàs, S. Gul, M. Ling, C. Blackman, J. Yano, A. Walsh and J. R. Durrant, *Chem. Sci.*, **2019**, 10, 5667–5677.
13. G. Panomsuwan, A. Watthanaphanit, T. Ishizaki and N. Saito, *Phys. Chem. Chem. Phys.*, **2015**, 17, 13794–13799.
14. W. Tu, Y. Xu, J. Wang, B. Zhang, T. Zhou, S. Yin, S. Wu, C. Li, Y. Huang, Y. Zhou, Z. Zou, J. Robertson, M. Kraft and R. Xu, *ACS Sustainable Chem. Eng.*, **2017**, 5, 7260−7268.
15. L. Shi, L. Yang, W. Zhou, Y. Liu, L. Yin, X. Hai, H. Song and J. Ye, *Small*, **2018**, 14, 1703142.

Chapter 1. Defect State-Induced Efficient Hot Electron Transfer in Au Nanoparticles/Reduced TiO_2 Mesocrystal Photocatalysts

1. Introduction

Coupling metal nanoparticles (NPs) showing surface plasmon resonance (SPR) with wide bandgap semiconductors to construct visible-light responsive plasmonic photocatalysts has been demonstrated as an effective strategy for efficient utilization of solar energy in photocatalytic reactions.[1] SPR arises from the collective oscillations of the electrons on the surface of the metal NPs, and the plasmon-excited hot electrons transfer to the CB of the adjacent semiconductor by overcoming the Schottky barrier, promoting the separation of electron–hole pairs.[2] However, the high Schottky barrier at the metal/semiconductor interface is a great hurdle for efficient hot ET, resulting in a low quantum efficiency, thereby severely restricting the application of plasmonic photocatalysts.[3] The utilization of hot electrons with energies lower than the Schottky barrier height (ϕ_B) may be the key to break this bottleneck. Recently, a few researchers proposed a tunneling mechanism for hot ET in some photovoltaic systems such as Au particles embedded in TiO_2 nanosheets[4] and Au nanorods fabricated on a Ti/Si double layer.[5] In addition, hot electron transport via DSs was suggested for the photodecomposition of acetaldehyde by TiO_2-coated Au nanocages.[6] In these systems, hot electrons with energies lower than ϕ_B are proposed to transfer to the CB of TiO_2 by tunneling through the Schottky barrier. Unfortunately, follow-up studies showed that the possibility of such hot electron tunneling is much lower than that of overbarrier transfer.[7] As a result, developing a novel strategy for the utilization of hot electrons with energies lower than ϕ_B to realize an efficient hot ET in the plasmonic photocatalyst system has been regarded as one of the big challenges in plasmonic photocatalysis.

Herein, we employ single-particle PL spectroscopy to investigate hot ET at the Au/TiO_2 interface. Combined with FDTD simulations, we demonstrate that

introduction of DSs in TiO_2 of Au/TiO_2 can build up a new channel for hot electrons with energies lower than ϕ_B to transfer to TiO_2, leading to an enhanced photocatalytic activity in the degradation of MB.

2. Experimental Section

Preparation of TMC. TMC was prepared from a precursor solution of TiF_4, H_2O, NH_4NO_3 and NH_4F (molar ratio = 1:117:6.6:4).[8] The above precursor was placed on a silicon wafer to form a thin layer with thickness no more than 1 mm. Then, the precursor solution was calcined in the air using a heating rate of 10 °C min^{-1} at 500 °C for 2h. At last, the obtained powders were calcined at 500 °C in the oxygen atmosphere for 8 h to completely remove the surface residue.

Preparation of reduced TMC (RTMC). RTMC was prepared by reducing TMC using $NaBH_4$. In detail, 60 mg of as-prepared TMC was mixed with 20 mg of $NaBH_4$ and the mixture was ground for 10 min thoroughly. Then the mixture was calcined at 350 °C in the argon atmosphere for 20 min. After naturally cooling down to the room temperature, the obtained powders were washed with Milli-Q ultrapure water several times to remove unreacted $NaBH_4$, and dried at 60 °C. Finally, RTMC with blue color was obtained.

Preparation of Au NPs. 1.5 mL of $HAuCl_4$ solution (1 wt.%) was dissolved in 99 mL of Milli-Q ultrapure water in a three-neck round-bottom flask which was equipped with a reflux condensing tube and heated to 100 °C. Under vigorous stirring, 1.2 mL of sodium citrate (1 wt.%) was added, and the reaction mixture was maintained at the boiling temperature for further 30 min before cooling down to room temperature. Finally, the colloidal solution of Au NPs was obtained.[9]

Preparation of Au/TMC and Au/RTMC. 20 mg of TMC was mixed with 40 mL of Au colloidal solution and sonicated for 2 min. The solvent of this suspension was evaporated by a rotary evaporator and then the obtained powders were calcined in air using a heating rate of 10 °C min^{-1} at 500 °C for 0.5 h. The powders were again dispersed in water, sonicated in an ultrasonic bath, and centrifuged at 9500 rpm to

remove the weakly attached Au NPs. Finally dried at 60 °C, Au/TMC was obtained. Au/RTMC was prepared by following the same method as Au/TMC, except for replacing TMC with RTMC.

Characterization. The samples were characterized using X-ray diffraction (XRD, Rigaku, Smartlab; operated at 40 kV and 200 mA, Cu Kα source), scanning electron microscopy (SEM, JEOL, JSM-6330FT), high resolution transmission electron microscopy (HRTEM, JEOL, JEM 3000F; operated at 300 kV), The X-ray photoelectron spectroscopy (XPS) measurements were carried out on a PHI X-tool 8ULVAC-PHI instrument. The steady-state UV−vis diffuse reflection spectra (DRS) were measured on a UV−vis−NIR spectrophotometer (Jasco, V-570) at room temperature. The Photoelectron yield spectroscopy (PYS) was carried out at excitation photon energies in the range of 4.0 to 9.0 eV with D2 lamp using a Bunkou-keiki BIPKV202GD in vacuum.

Photocatalytic degradation of MB. For typical photocatalytic runs, 2 mg of as-prepared sample was dispersed into a mixture of 2 mL of MB aqueous solution (1.0×10^{-5} M) and 0.5 mL of tert-butyl alcohol (TBA) in a quartz cuvette with circulating cooling water to keep the reaction temperature constant. Prior to illumination, the mixed suspension was magnetically stirred in the dark for 30 min to obtain the adsorption−desorption equilibrium. Subsequently, the suspension with continuous stirring was irradiated under a Xe lamp (Asahi Spectra, HAL-320; 350 mW cm^{-2}) equipped with a 420 nm cutoff filter at room temperature. After the visible illumination, the sample was centrifuged at 9500 rpm to remove the particles. The concentration of unreacted MB molecules was analyzed by a UV−vis spectrophotometer (Shimadzu, UV-3100) at the characteristic wavelength. After the last photodegradation run, the precipitates after centrifugation were recovered, washed and dried, and reused in four times to test the photocatalytic stability of as-prepared samples.

Single-Particle PL Measurements by Confocal Microscopy. Samples were dispersed on the cover glasses in prior to the single-particle PL measurements. In detail, the cover glasses were firstly cleaned by sonication in a 20% detergent solution for 7 h, followed

by repeated washing with warm water 5 times. The colloidal solution of Au NPs was centrifuged and then washed by water several times. Au NPs, Au/TMC and Au/RTMC were dispersed in water to form a well-dispersed aqueous suspension. Subsequently, the above suspensions were spin-coated on the cleaned cover glass. The cover glass was annealed at 80 °C for 1 h to immobilize the particles on the surface.

Single-particle PL images and spectra were recorded by using an objective scanning confocal microscope system (PicoQuant, MicroTime 200) coupled with an Olympus IX71 inverted fluorescence microscope. The samples were excited through an oil-immersion objective lens (Olympus, UplanSApochromat, 100×, 1.4 NA) by a circular-polarized 488 nm continuous wave (CW) laser controlled by a PDL-800B driver (PicoQuant). Typical excitation power for the PL measurements was 300 μW at the sample. The emission from the sample was collected by the same objective and detected by a single-photon avalanche photodiode (SPAD, Micro Photon Devices, PDM 50CT) through a dichroic beam splitter (Chroma, 488rdc) and a long pass filter (Chroma, HQ513CP). For the spectroscopy, only the emission that passed through a slit entered the imaging spectrograph (Acton Research, SP-2356) that was equipped with an electron-multiplying charge-coupled device (EMCCD) camera (Princeton Instruments, ProEM). The spectra were typically integrated for 10 s. The spectrum detected by the EMCCD camera was stored and analyzed by using a personal computer. It should be noted that the PL spectra in the thesis do not fully reproduce real spectral shapes of the samples, because the above long pass filter (> 513 nm) was inserted to completely remove the excitation light. All the experimental data were obtained at room temperature.

FDTD calculations. The enhancement of electric field at the interface of Au/TiO_2 was calculated by using a software package, FDTD Solutions 8.19 (Lumerical Solutions, Inc.). During simulations, an electromagnetic pulse in the wavelength range from 400 to 700 nm was launched into a box containing a target nanostructure. The override mesh cell size used was 1 × 1 × 1 nm^3. The model employed in this chapter is a gold nanosphere of 50 nm in diameter supported on a TiO_2 nanosheet of 20 nm in thickness.

The optical constant of bulk gold measured by Johnson and Christy[10] was used in the simulation, while that of TiO_2 was from Handbook of Optical Constants of Solids[11]. The refractive index of the medium (water) was set to be 1.33.

3. Results and Discussion

Strong XRD peaks (Figure 1) indicate that the TMC is highly crystallized with anatase structures (JCPDS No. 21-1272). The SEM image (Figure 2a) shows that the pristine TMC system presents a plate-like structure with a size of 3–5 μm and a thickness of 100–300 nm. Compared with the pristine TMC, RTMC shows no structural change. After the thermal treatment with Au NPs, Au NPs with a size of 30–90 nm are found to be randomly distributed on the basal surface of the RTMC (Figure 2b). The HRTEM images taken at the Au/RTMC interface (Figures 2c and d) show the structural information in detail. The well-identified lattice spacings of 0.189 nm and 0.25 nm (Figure 2d) correspond to the (200) crystal plane of anatase TiO_2 and the (111) crystal plane of cubic Au, respectively.[9] For comparison, Au/TMC was also prepared to present a similar morphology to Au/RTMC.

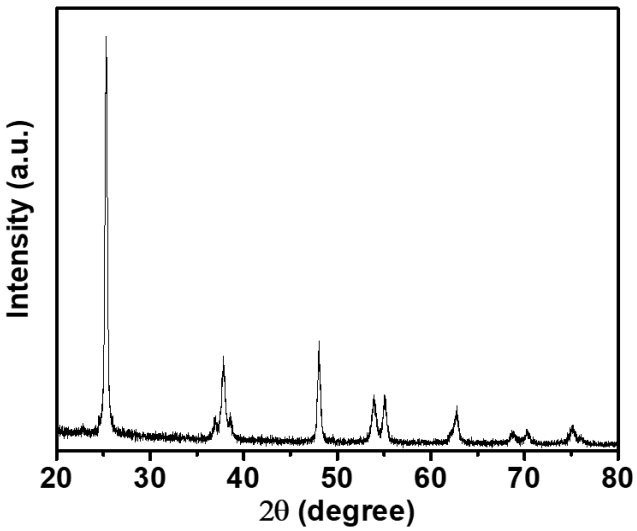

Figure 1. XRD pattern of TMC.

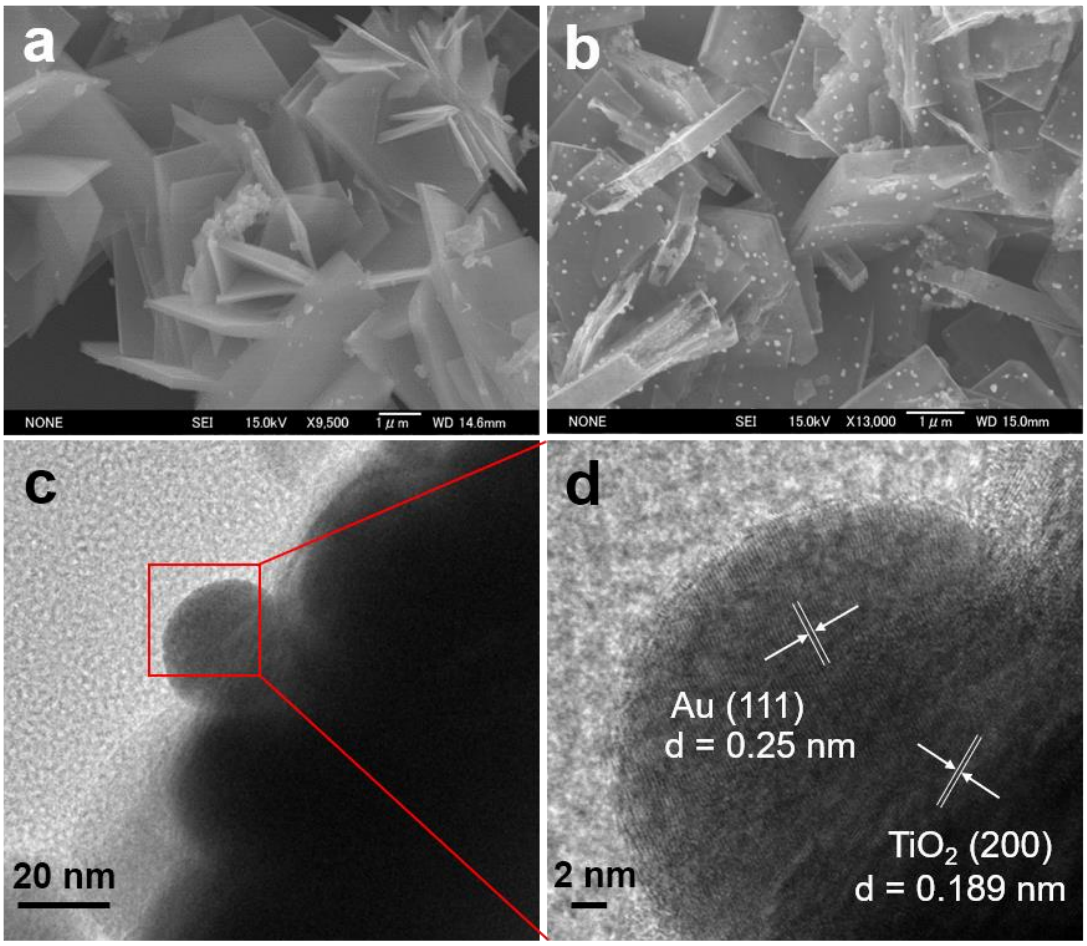

Figure 2. SEM images of (a) TMC) and (b) Au/RTMC. (c and d) HRTEM images of Au/RTMC.

The presence of Ti^{3+} defects in RTMC was confirmed by XPS (Figure 3) to demonstrate the existence of oxygen vacancies (V_os) due to the electrostatic balance.[12] After loading Au NPs, the amount of defects decreased, because the calcination process oxidized Ti^{3+} species back to Ti^{4+} species by O_2 in air.[13] Both defects and Au NPs can significantly modify the optical properties of TMC. As shown in Figure 4a, compared with the pristine TMC, RTMC shows an increasing absorption band in the visible-light region, and Au/TMC displays a broad SPR band at 535 nm. It is reported that the defects in reduced TiO_2 add localized states below the CB.[14,15] The electronic transitions from the VB to the DSs and from the DSs to the CB are responsible for the visible-light absorption of reduced TiO_2.[16,17] Au/RTMC shows higher visible-light absorption due to a combination of DS-induced electronic transitions with the SPR excitation of Au NPs.

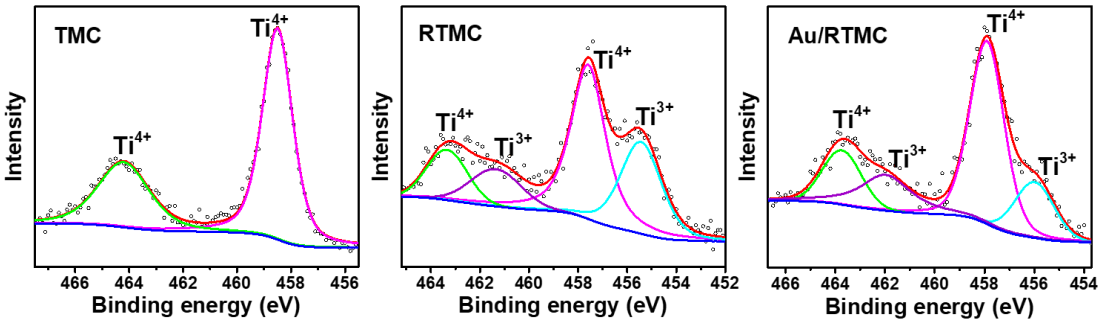

Figure 3. Ti 2p XPS spectra of TMC, RTMC, and Au/RTMC.

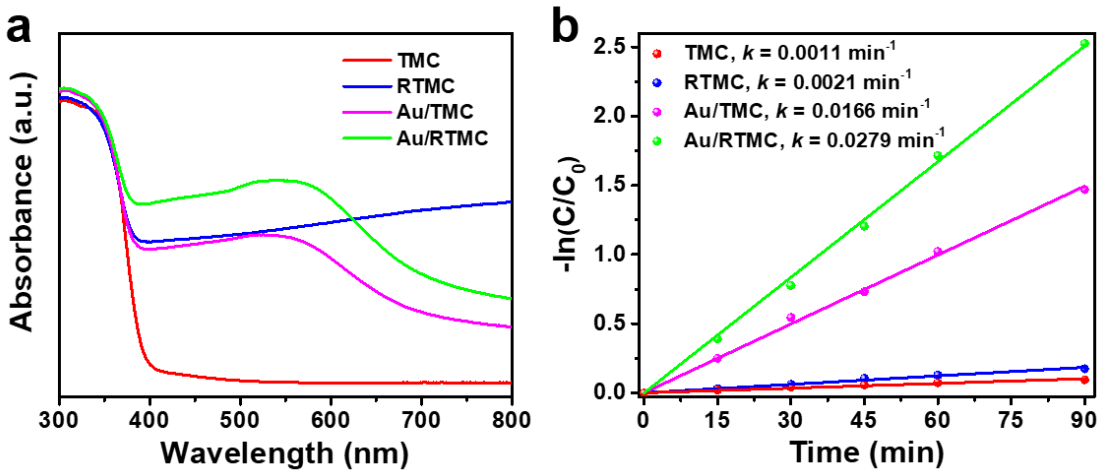

Figure 4. (a) UV−vis DRS. (b) Kinetic linear fitting curves for photocatalytic degradation of MB solution under visible-light irradiation ($\lambda < 420$ nm).

The photocatalytic degradation of MB solution under visible-light irradiation was carried out to evaluate the activity of the as-prepared photocatalysts. In order to eliminate the contribution of hydroxyl radicals (•OH) to the degradation of MB, TBA as an •OH scavenger was introduced into the reaction mixture.[18] Therefore, only superoxide radicals ($O_2^{\bullet-}$) that originated from photogenerated electrons contributed to the degradation of MB.[19] Figure 4b shows the corresponding time profiles of $-\ln(C/C_0)$. According to the Langmuir–Hinshelwood model, the apparent first-order-rate constant (k) for each photocatalyst was calculated. The pristine TMC shows negligible photocatalytic degradation of MB (k = 0.0011 min^{-1}) because it cannot absorb visible light. RTMC shows a very limited photocatalytic degradation rate (k = 0.0021 min^{-1}) although it has a considerable visible-light absorption. This is due to the short lifetimes and low mobilities of the photogenerated electrons in the DSs.[20] Conversely, Au/TMC

shows a significantly enhanced degradation rate (k = 0.0166 min^{-1}), owing to the anisotropic migration of the electrons injected from the excited Au NPs.[9] Considering the low photocatalytic activity of the RTMC, it was supposed that the photocatalytic activity of Au/RTMC would not increase very much compared with Au/TMC. However, interestingly, the degradation rate for Au/RTMC (k = 0.0279 min^{-1}) shows an obvious enhancement of 68.1%. It turns out that the DSs in Au/RTMC may facilitate hot ET from Au NPs to the RTMC and thereby enhance the photocatalytic activity of Au/RTMC.

Single-particle PL microscopy was adopted to investigate the hot ET in the photocatalytic MB degradation by Au/RTMC. To exclude the effect of NP sizes on the hot ET,[21] we selected Au NPs with similar sizes in the measurements. Figure 5a shows the single-particle PL images of individual Au NPs. Compared with bare Au NPs, the brightness of the single-particle images of Au NPs in Au/TMC (Figure 5b) becomes weak, indicating that the PL is quenched by the TMC. For Au NPs in Au/RTMC, the PL is further quenched as shown in Figure 5c. Moreover, the single-particle PL images show small variations in intensity for each bare Au NP, AuNP in Au/TMC, and AuNP in Au/RTMC. This is because the PL intensity depends on the size and shape of single nanoparticles and is also influenced by the morphological heterogeneity.[22,23] To intuitively compare the intensities of PL, three representative PL spectra of bare AuNPs, Au NPs in Au/TMC and Au NPs in Au/RTMC are chosen to be shown in Figure 5d. According to Figure 5d, the quenching efficiencies of PL for Au NPs in Au/TMC and Au/RTMC are calculated to be 68% and 92%, respectively.

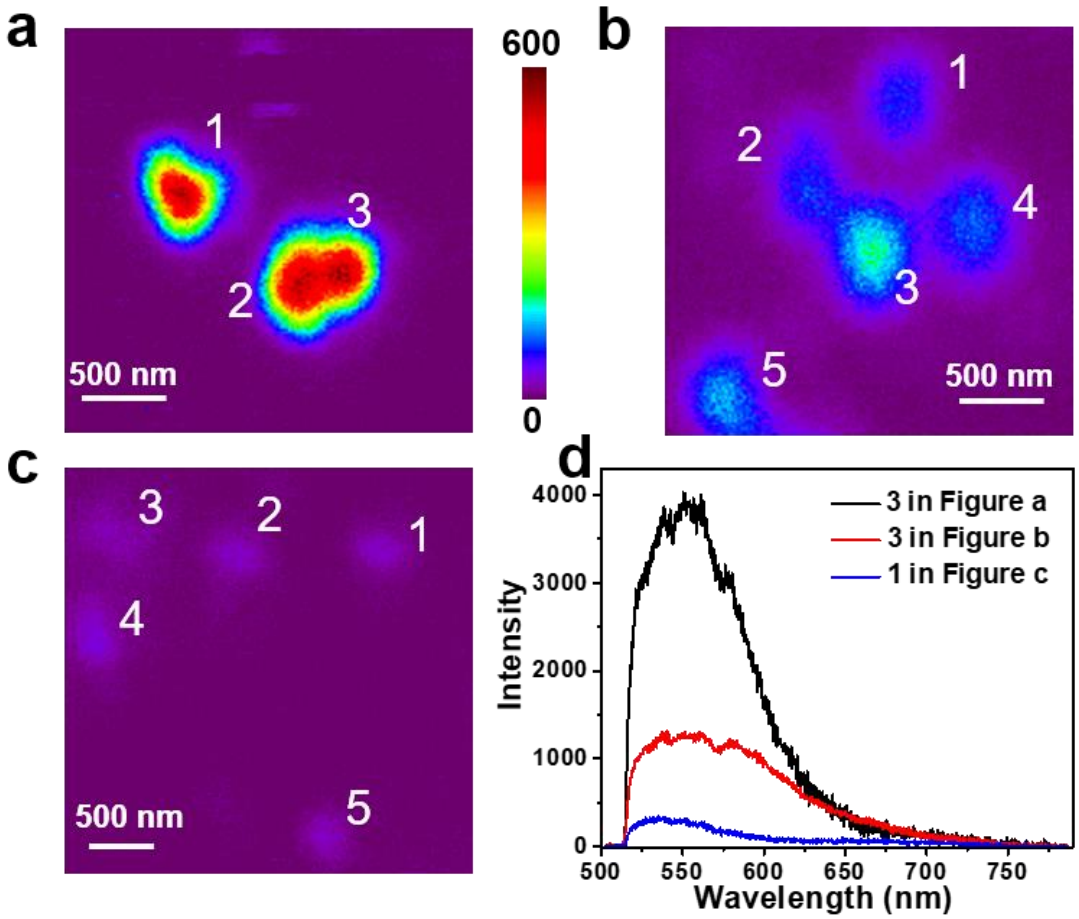

Figure 5. Single-particle PL images of (a) bare Au NPs, (b) Au NPs in Au/TMC, and (c) Au NPs in Au/RTMC. (d) Three representative PL spectra of individual Au NPs as shown in (a–c).

In our single-particle test, the interband transition of Au NPs was induced by 488 nm excitation to generate electron–hole pairs, which relaxed very efficiently through a fast interconversion with the SPR mode and subsequently decayed radiatively (red line, Figure 6a), leading to the PL images as observed above.[24] When Au NPs are loaded on the TMC, the band edges of the TiO_2 surface are bent upward to form a Schottky barrier at the Au/TMC interface. The hot electrons with energies higher than ϕ_B can overcome the Schottky barrier and transfer to the CB of TiO_2 (overbarrier, Figure 6b), resulting in CS (Figure 6a). The hot ET competes with the SPR emission, leading to PL quenching. Therefore, the enhanced PL quenching effect observed in the Au/RTMC system indicates that a more efficient ET is achieved in the presence of DSs. Therefore, the DSs open a new channel for the hot electrons with energies lower than ϕ_B to transfer to

the RTMC. First-principles simulations revealed that when Au atoms are settled on a stoichiometric TiO_2 surface, the interface states, which are mainly composed of Au 5d states mixed with the orbitals of adjacent Ti and O atoms, are derived.[2] Interestingly, in the case of Au atoms settled on an off-stoichiometric TiO_2 surface (with defects), Au atoms bind very strongly on the defect sites, leading to the formation of polarized covalent bonds between Au atoms and coordinatively unsaturated Ti atoms.[25] Such polarized covalent bonds are characterized by the charge transfer states (CTSs) derived from coupling of the interface states with the DSs.[26] In this case, as proposed in Figure 6b, the hot electrons with energies higher than ϕ_B transfer to the CB of the RTMC by the overbarrier mechanism. Meanwhile, the hot electrons with energies lower than ϕ_B can directly transfer to the DSs via the CTSs away from the limits of the Schottky barrier. As a result, a more efficient ET is realized.

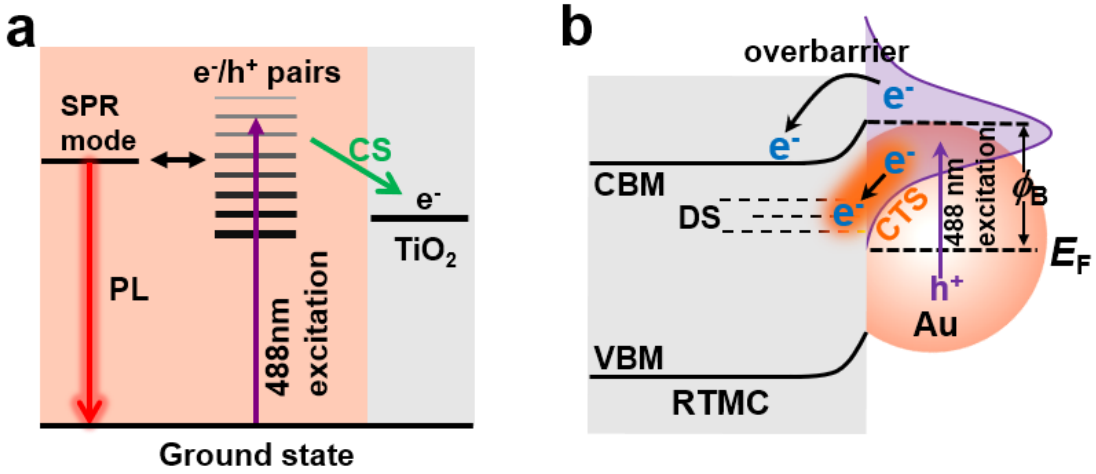

Figure 6. Schematic diagrams of (a) the mechanism for radiative decay of surface plasmon and (b) the hot ET at the Au/RTMC interface. E_F, Fermi level; CBM, CB minimum; VBM, VB maximum.

In addition to the more efficient hot ET, the enhancement of the local electric field can also occur at the Au/RTMC interface to accelerate the excitation of electrons in the DSs. To clarify this process in detail, the FDTD simulations were carried out to calculate the electric field enhancement in the Au/TiO_2 hybrid system. Under perpendicular polarization, the electric field intensity enhancement contour reveals a spatially confined "hot spot" at the Au/TiO_2 interface (Figure 7a). When Au/RTMC are

irradiated with visible light, the electrons in the VB of the RTMC can be excited to the DSs (pink electrons in Figure 7b). The lifetimes of these electrons are very short due to the fast recombination with the holes in the VB. Meanwhile, hot electrons with energies lower than ϕ_B transfer to the DSs through the CTSs (blue electrons). The DSs are located only 0.7–1.0 eV below the CBM,[16] to be covered by the energy of Au SPR. Therefore, the SPR-induced electric field is sufficient to further excite the trapped electrons in the DSs to the CB of TiO_2,[27–29] where they react with O_2 to produce $O_2^{\bullet-}$. The "hot" region is therefore the place where such excitation (DSs to CB) is largely boosted (Figure 7b) to inhibit the recombination of electrons and holes, leading to the enhanced photocatalytic performance of Au/RTMC in MB degradation.

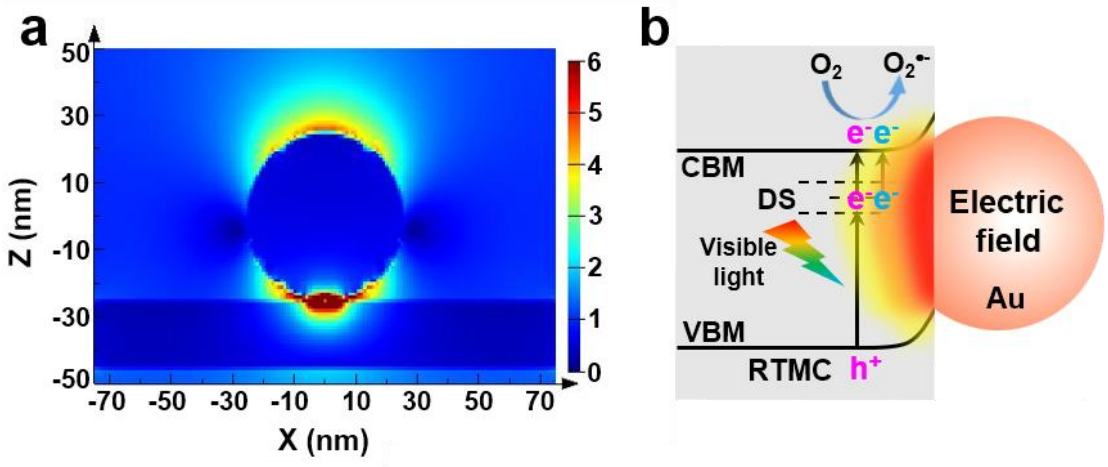

Figure 7. (a) Electric field intensity enhancement contours of the Au/TiO_2 hybrid system under the perpendicular polarized excitation. The color scale bar shows the relative increase in field enhancement $|E|/|E_0|$. (b) A schematic diagram of the electric field-induced excitations of electrons.

4. Conclusion

In summary, we have created DSs in the Au/TMC system to trap the hot electrons with energies lower than ϕ_B, leading to efficient hot ET at the interface. Moreover, under the effect of the SPR-induced electric field, these trapped hot electrons together with the excited electrons from the VB of the TMC can be further excited to the CB where they

react with O_2 to produce $O_2^{\bullet-}$, resulting in the enhanced photocatalytic degradation rate of MB. The above findings suggest that engineering of the DSs has great potential in the development of more efficient plasmonic metal–semiconductor composites for a wide range of photocatalytic applications.

5. References

1. S. Linic, P. Christopher and D. B. Ingram, *Nat. Mater.*, **2011**, 10, 911–921.
2. S. Wang, Y. Gao, S. Miao, T. Liu, L. Mu, R. Li, F. Fan and C. Li, *J. Am. Chem. Soc.*, **2017**, 139, 11771–11778.
3. Y. Shiraishi, N. Yasumoto, J. Imai, H. Sakamoto, S. Tanaka, S. Ichikawa, B. Ohtani and T. Hirai, *Nanoscale*, **2017**, 9, 8349–8361.
4. S. Mubeen, G. Hernandez-Sosa, D. Moses, J. Lee and M. Moskovits, *Nano Lett.*, **2011**, 11, 5548–5552.
5. M. Moskovits, *Science*, **2011**, 332, 676–677.
6. R. Kodiyath, M. Manikandan, L. Liu, G. V. Ramesh, S. Koyasu, M. Miyauchi, Y. Sakuma, T. Tanabe, T. Gunji, T. D. Dao, S. Ueda, T. Nagao, J. Ye and H. Abe, *Chem. Commun.*, **2014**, 50, 15553–15556.
7. C. Clavero, Nat. Photonics, 2013, 8, 95–103.
8. Z. Bian, T. Tachikawa and T. Majima, *J. Phys. Chem. Lett.*, **2012**, 3, 1422−1427.
9. Z. Bian, T. Tachikawa, P. Zhang, M. Fujitsuka and T. Majima, *J. Am. Chem. Soc.*, **2014**, 136, 458–465.
10. P. B. Johnson and R. W. Christy, *Phys. Rev. B*, **1972**, 6, 4370–4379.
11. E. D. Palik, *Handbook of Optical Constants of Solids*, Academic Press, San Diego, **1997**.
12. X. Jiang, Y. Zhang, J. Jiang, Y. Rong, Y. Wang, Y. Wu and C. Pan, *J. Phys. Chem. C*, **2012**, 116, 22619–22624.
13. G. Li, Z. Lian, X. Li, Y. Xu, W. Wang, D. Zhang, F. Tian and H. Li, *J. Mater. Chem. A*, **2015**, 3, 3748–3756.
14. X. Chen, L. Liu, P. Y. Yu and S. S. Mao, *Science*, **2011**, 331, 746–750.

15. Y. Zhou, C. Chen, N. Wang, Y. Li and H. Ding, *J. Phys. Chem. C*, **2016**, 120, 6116–6124.
16. A. Naldoni, M. Allieta, S. Santangelo, M. Marelli, F. Fabbri, S. Cappelli, C. L. Bianchi, R. Psaro and V. D. Santo, *J. Am. Chem. Soc.*, **2012**, 134, 7600–7603.
17. J. Xue, X. Zhu, Y. Zhang, W. Wang, W. Xie, J. Zhou, J. Bao, Y. Luo, X. Gao, Y. Wang, L. Jang, S. Sun and C. Gao, *ChemCatChem*, **2016**, 8, 2010–2014.
18. O. Elbanna, P. Zhang, M. Fujitsuka and T. Majima, *Appl. Catal., B*, **2016**, 192, 80–87.
19. Q. Zhang, J. Deng, Z. Xu, M. Chaker and D. Ma, *ACS Catal.*, **2017**, 7, 6225–6234.
20. S. K. Cushing, F. Meng, J. Zhang, B. Ding, C. K. Chen, C. Chen, R. Liu, A. D. Bristow, J. Bright, P. Zheng and N. Wu, *ACS Catal.*, **2017**, 7, 1742–1748.
21. K. Qian, B. C. Sweeny, A. C. Johnston-Peck, W. Niu, J. O. Graham, J. S. DuChene, J. Qiu, Y.-C. Wang, M. H. Engelhard, D. Su, E. A. Stach and W. D. Wei, *J. Am. Chem. Soc.*, **2014**, 136, 9842–9845.
22. X. Shi, Z. Lou, P. Zhang, M. Fujitsuka and T. Majima, *ACS Appl. Mater. Interfaces*, **2016**, 8, 31738–31745.
23. Z. K. Zheng, T. Tachikawa and T. Majima, *Chem. Commun.*, **2015**, 51, 14373–14376.
24. Z. Zheng, T. Tachikawa and T. Majima, *J. Am. Chem. Soc.*, **2014**, 136, 6870–6873.
25. S. Laursen and S. Linic, *J. Phys. Chem. C*, **2009**, 113, 6689–6693.
26. P. Schlexer, A. R. Puigdollers and G. Pacchioni, *Phys. Chem. Chem. Phys.*, **2015**, 17, 22342–22360.
27. D. B. Ingram and S. Linic, *J. Am. Chem. Soc.*, **2011**, 133, 5202–5205.
28. Z. Liu, W. Hou, P. Pavaskar, M. Aykol and S. B. Cronin, *Nano Lett.*, **2011**, 11, 1111–1116.
29. A. Naldoni, F. Fabbri, M. Altomare, M. Marelli, R. Psaro, E. Selli, G. Salviati and V. D. Santo, *Phys. Chem. Chem. Phys.*, **2015**, 17, 4864–4869.

Chapter 2. The Role of Nitrogen Defects in Graphitic Carbon Nitride for Visible-Light-Driven Hydrogen Evolution

1. Introduction

Photocatalytic H_2 evolution from water driven by solar light is regarded as one of the most promising strategies to mitigate global warming and energy crisis. As a typical visible-light-responsive photocatalyst, CN has drawn wide attention due to its easy availability, low-cost, good stability, and excellent electronic properties.[1,2] However, the absorption of CN is restricted in the blue region of visible light by its wide bandgap of ~2.7 eV. Hence, various methods such as introducing heteroatoms[3–5] or defects,[6,7] especially N defects (V_ns[8–16] or cyano groups[17–25]), have been applied to extend the light absorption region of CN. Very recently, Yu et al.[18] and Niu et al.[22] independently realized the extension of the absorption region of CN to ~700 nm by introducing V_ns and cyano groups simultaneously. However, such a wider absorption range does not guarantee better photocatalytic activity under visible-light irradiation. Unfortunately, only a limited enhancement of the H_2 evolution rate was observed even for the optimized samples. This has motivated us to explore the underlying mechanism of this dilemma.

In essence, besides light-harvesting, the photocatalytic activity of a given semiconductor strongly depends on electron–hole transfer, which is a key rate-determining step in the photocatalytic reactions.[26] Moreover, the electronic structure plays a crucial role in governing the electron–hole transfer dynamics, which has not been fully understood for CN due to the complicated nature of the mid-gap states induced by defects. In this regard, previous reports show that V_ns introduce extra electronic states above the VB[11,27] and cyano groups narrow the bandgap of CN,[18,22,23,28] resulting in the absorption extension of the DCN. However, visual and specific descriptions of N defects contributing to the electronic structure changes, thus determining the electron–hole transfer, have not been taken into account, which hinders

a comprehensive understanding of the photocatalytic activity of DCN. Therefore, obtaining insights into such a process has emerged as one of the most important challenges in the photocatalysis of DCN.

In this chapter, the effects of N defects on the electronic structure and charge transfer of CN are analyzed in detail by UV−vis, VB XPS, and DFT calculations. As a result, the negative factors introduced by N defects, which are easily covered by the positive effect of the wide light-harvesting range, are pointed out to clarify the in-depth mechanism of the limited activity enhancement of DCN for H_2 evolution.

2. Experimental Section

Preparation of CN and DCN. DCN was synthesized via a KOH-assisted thermal polymerization method.[18] Briefly, 15 g of urea was dissolved with stirring into the KOH solution (1.0 g KOH in 30 mL of H_2O), and then the as-obtained solution was evaporated to dryness in an oven at 80 °C overnight. The solid mixtures of urea and KOH were then calcined at 550 °C in a muffle furnace for 4 h using a heating rate of 2 °C min^{-1}. For comparison, CN was also synthesized parallelly in the absence of KOH.

Characterization. The samples were characterized by XRD, SEM, XPS, and UV−vis DRS as in Chapter 1. Fourier transformed infrared (FTIR) measurements were conducted using FT/IR-4100 (JASCO, Japan) and collected in the ATR mode. Electron paramagnetic resonance (EPR) spectra were recorded on a JEOL JES-RE2X electron spin resonance spectrometer at room temperature.

Photocatalytic H_2 evolution. 3 mg of the sample was dispersed in 5 mL triethanolamine (TEOA, as a sacrificial agent)-H_2O solution (V_{TEOA}:V_{H_2O} = 1:4) and added into a 35 mL cylinder reactor. Then, 3 wt.% (respect to Pt, acting as a cocatalyst) $H_2PtCl_6 \cdot 6H_2O$ was deposited onto the photocatalyst by the photodeposition method. The reactor was sealed, and then bubbled with argon through the reactor for 30 min to completely remove the dissolved oxygen and ensure the reactor was in an anaerobic condition. Subsequently, the suspension with continuous stirring was irradiated under a UV-LED source (Asahi Spectra, POT-365, 100 mW cm^{-2}) or a Xe lamp (Asahi

Spectra, HAL-320; 350 mW cm^{-2}) equipped with a 420 nm or 460 nm cutoff filter at room temperature. H_2 production was measured by using a Shimadzu GC-8A gas chromatograph equipped with an MS-5A column and a thermal conductivity detector. The AQEs for H_2 production at 420, 460, 500, and 560 nm were calculated via the following equation: AQE = (2 × number of H_2 molecules/number of incident photons) × 100%.

DFT calculation. All calculations were carried out using the CASTEP code based on the plane-wave pseudopotential method.[29] Nonlocal exchange and correlation energies were treated with the Perdew−Burke−Ernzerhof (PBE) functional, which was based on the generalized gradient approximation (GGA). Taking into account the long-range effect of the van der Waals (vdW) force, the vdW interactions were added with the DFT-D method of Grimme.[30] A 500 eV cutoff was assigned to the plane-wave basis set and the Brillouin zone was sampled by 3 × 3 × 4 *k*-points. In the geometry optimization process, the energy convergence tolerance and maximum force were set to be 5.0×10^{-6} eV per atom and 0.01 eV $Å^{-1}$, respectively. We applied a scissor operator to match the experimental bandgap values.

3. Results and Discussion

The XRD patterns of CN (Figure 1a) show two characteristic peaks at 27.5° and 13.1°, which are, respectively, attributed to the (002) interlayer stacking of conjugated aromatic segments and the (100) in-plane structural packing motifs of tri-*s*-triazine units.[9,12,13] For DCN, it is clearly observed that the former peak shifts slightly to 27.8°, indicating the decrease of interlayer stacking distance.[21,27] Moreover, both peaks of DCN become broader and weaker than those of CN, suggesting the lowered order degree of in-plane structural packing due to the presence of defects.[9,21,27] The successful introduction of N defects can be directly evidenced by elemental analysis (EA) and XPS. As shown in Table 1, the smaller N/C atomic ratio in DCN than that in CN indicates the presence of V_ns in DCN. To further determine the location of V_ns, the electronic states of N were tested by XPS. The N 1s XPS spectra (Figure 1b) of CN

show three fitting peaks assignable to C–N=C (N_{2C}, 398.5 eV), N–$(C)_3$ (N_{3C}, 399.5 eV), and C–N–H_x (x = 1 or 2, 400.9 eV).[15,22] Once V_ns are introduced, the ratio of N_{2C} to N_{3C} drops drastically from 2.51 to 1.79, manifesting that V_ns are preferentially introduced at the N_{2C} (two-coordinated N) site. Besides, it is noteworthy that the N_{3C} peak of DCN shows a slightly lower energy shift than that of CN because the loss of N atoms (formation of V_ns) would leave extra electrons, which are redistributed to adjacent N_{3C} atoms through the delocalized π-conjugated networks of CN.[21] Additional K ions (3.78 at%) are also detected by XPS. It is reported that the incorporated K ions do not take part in the electronic structure of DCN, but improve the conductivity, which would be in favor of carrier transfer.[31] The existence of cyano groups in DCN is directly confirmed by the FTIR spectra (Figure 1c), in which a new peak at 2177 cm^{-1}, corresponding to the asymmetric stretching vibration of the cyano groups,[18] is observed. According to previous reports, cyano groups are formed by breaking the N–C=N heterocycles during the thermal treatment process.[25,28] Finally, the N defects were examined by the EPR spectroscopy, a tool for probing unpaired electrons in materials. Taking CN with rare defects as a reference, apparently an enhanced EPR signal at g = 2.003 was observed in DCN (Figure 1d), which can be attributed to an unpaired electron on the C atoms of the tri-*s*-triazine units.[13] Based on the above structural analysis, the structures of CN and DCN are given in Figure 2.

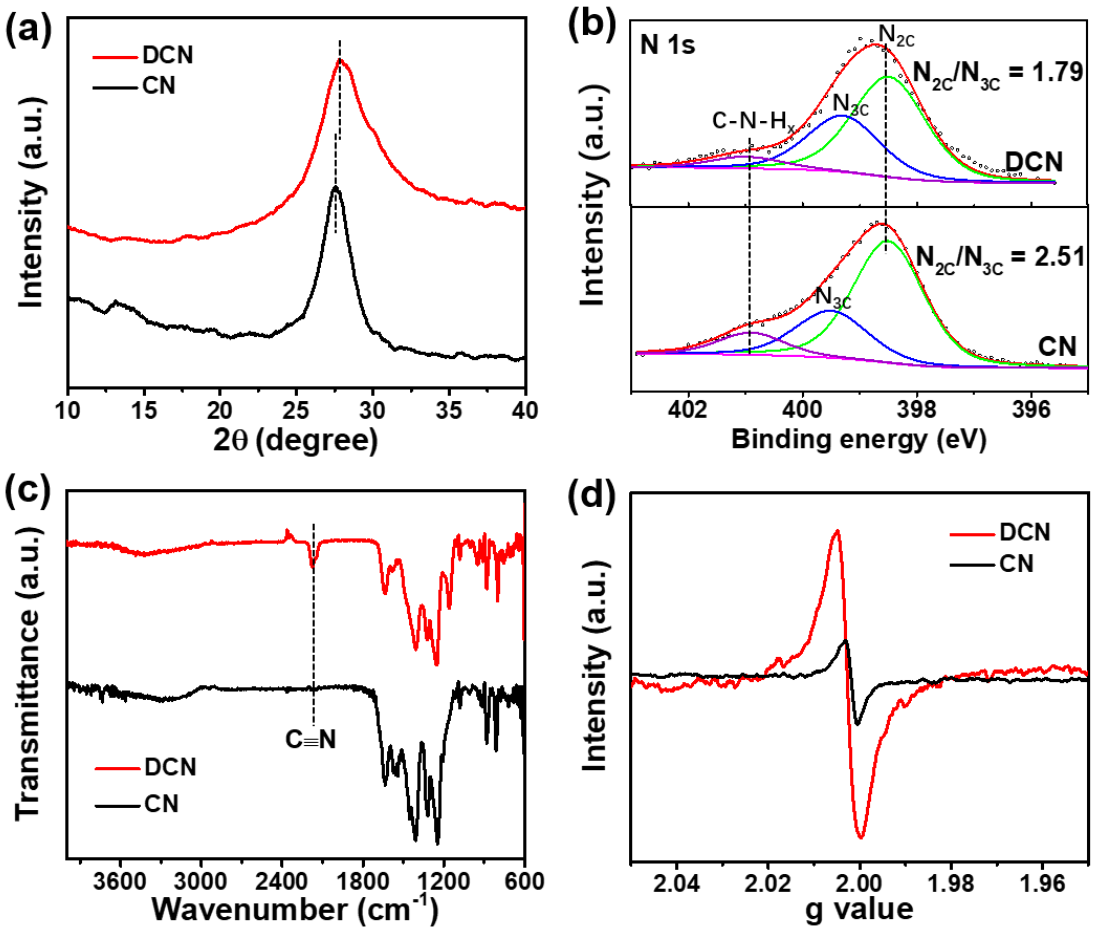

Figure 1. (a) XRD patterns, (b) N 1s XPS spectra, (c) FTIR spectra, and (d) EPR spectra of CN and DCN.

Table 1. N/C atomic ratios of CN and DCN determined by EA.

Sample	N (wt.%)	C (wt.%)	H (wt.%)	N/C (at.)
CN	57.54	32.66	1.95	1.51
DCN	56.18	33.73	2.08	1.43

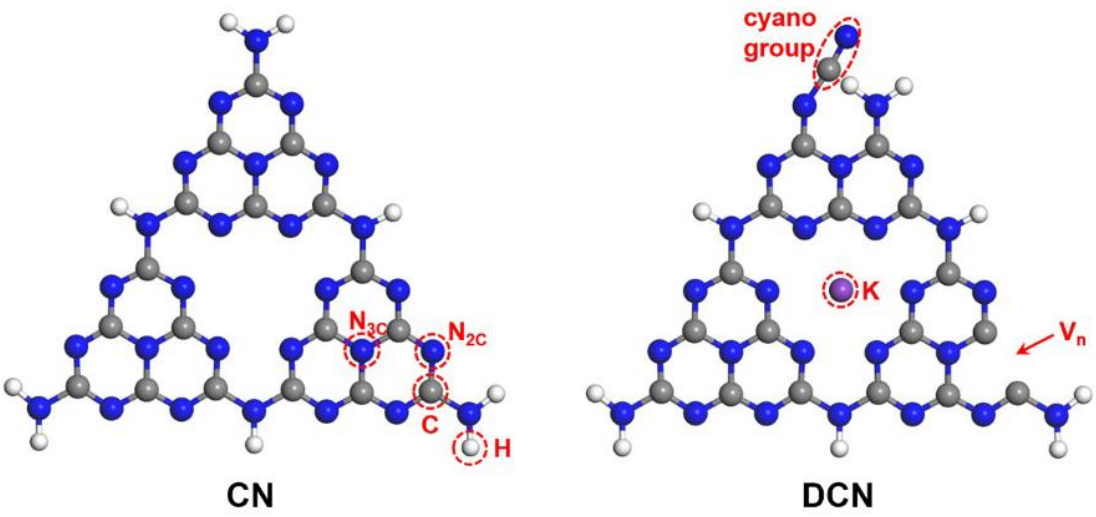

Figure 2. Schematic illustrations of the atomic structures of CN and DCN.

The electron redistribution induced by N defects as shown above suggests that a different electronic structure may be achieved when N defects are introduced. Therefore, the N defect-induced electronic structure change was investigated by UV−vis DRS and VB XPS. As shown in UV−vis DRS spectra (Figure 3a), the introduction of N defects not only red-shifts the intrinsic absorption edge of CN to ~500 nm, but also adds a shoulder on the absorption edge to further extend the absorption to ~700 nm. As a result, the bandgap of DCN is determined to be ~2.70 eV with a sub-gap of ~1.88 eV corresponding to the absorption edge of the add-on shoulder (Figure 3b). Meanwhile, the bandgap of CN is determined to be ~2.91 eV. The density of states (DOS) of the VB of CN and DCN were measured by VB XPS (Figure 3c), The VBM of CN occurs at ~2.33 eV below the E_F, close to the previous report.[32] For DCN, two continuum states overlapping with the VB edge (the inset in Figure 3c) result in a VB tailing to ~1.70 eV; thus they are often also known as band tail states.[33] Combined with the bandgap values, a schematic illustration of the electronic structures of CN and DCN can be obtained as in Figure 3d.

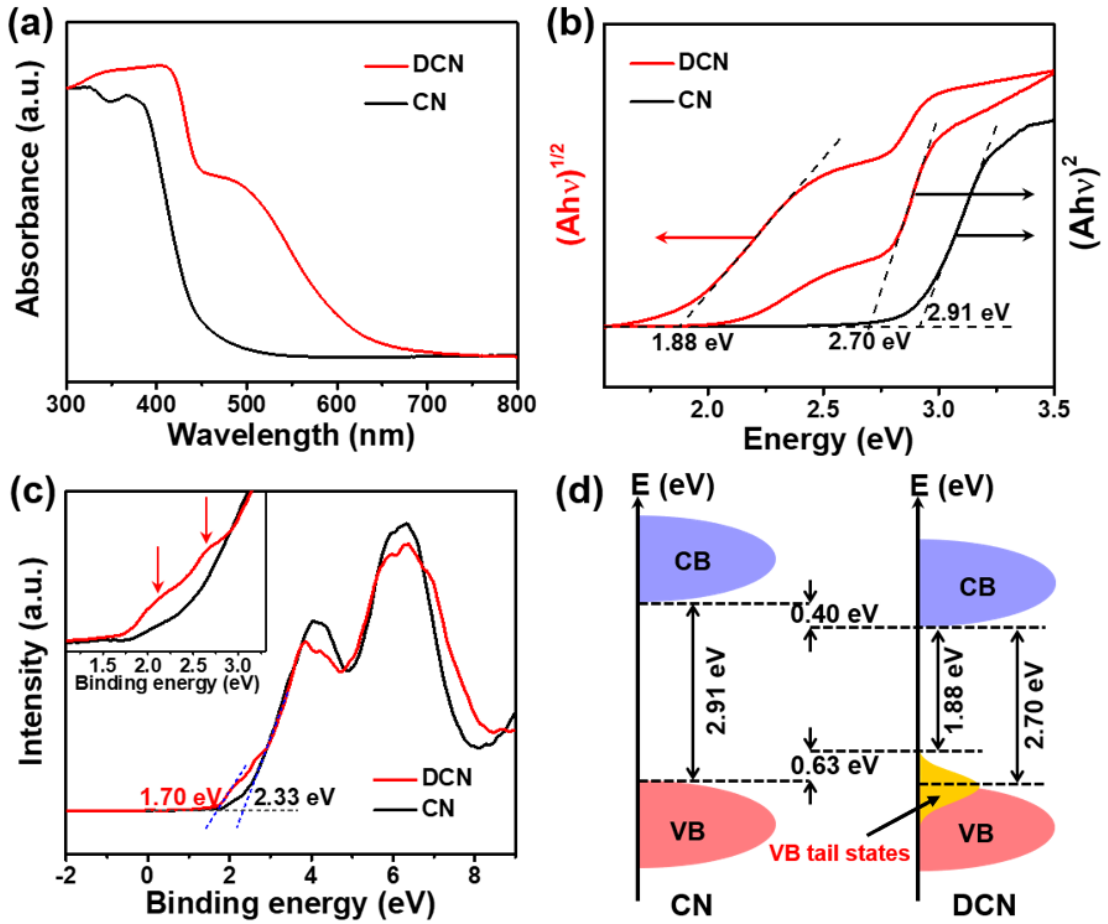

Figure 3. (a) UV−vis DRS, (b) Tauc plots for the bandgap calculation, (c) VB XPS spectra (the two red arrows mark the two continuum electronic states), and (d) schematic illustrations of the electronic structures of CN and DCN.

In order to understand the effect of N defects on the electronic structure of CN, the DOS for CN, CN with V_n, and CN with cyano group were calculated using first-principles DFT. Given that the incorporated K ions do not take part in the electronic structure of DCN,[31] the K ions were not considered during calculation. According to Figure 4a, CN yields a bandgap of ~2.46 eV, close to the experimentally observed bandgap in this work. When a N_{2C} vacancy is introduced, by carefully monitoring the electronic structure change of the VB, it is interesting to find that two continuum mid-gap states overlap with the VB edge, forming a VB tail, in good agreement with the results of VB XPS. Such VB tail states (V_n states) are delocalized and mainly hybridized from C p orbitals and N p orbitals from the VB states. Moreover, the CB and the intrinsic VB energies are lowered parallelly. As a result, the presence of V_ns

almost does not change the intrinsic bandgap of CN, but produces a sub-gap of ~1.99 eV (Figure 4b). Therefore, it is logical to anticipate that the red shift of the intrinsic absorption edge of CN observed in the UV−vis DRS spectrum is caused by the cyano groups. This assumption has been confirmed by our calculation on CN with one cyano group. It is found that the CB energy is lowered while the VBM remains unchanged, leading to a narrowed bandgap of ~2.14 eV, consistent with the experimental results in previous reports.[23,28]

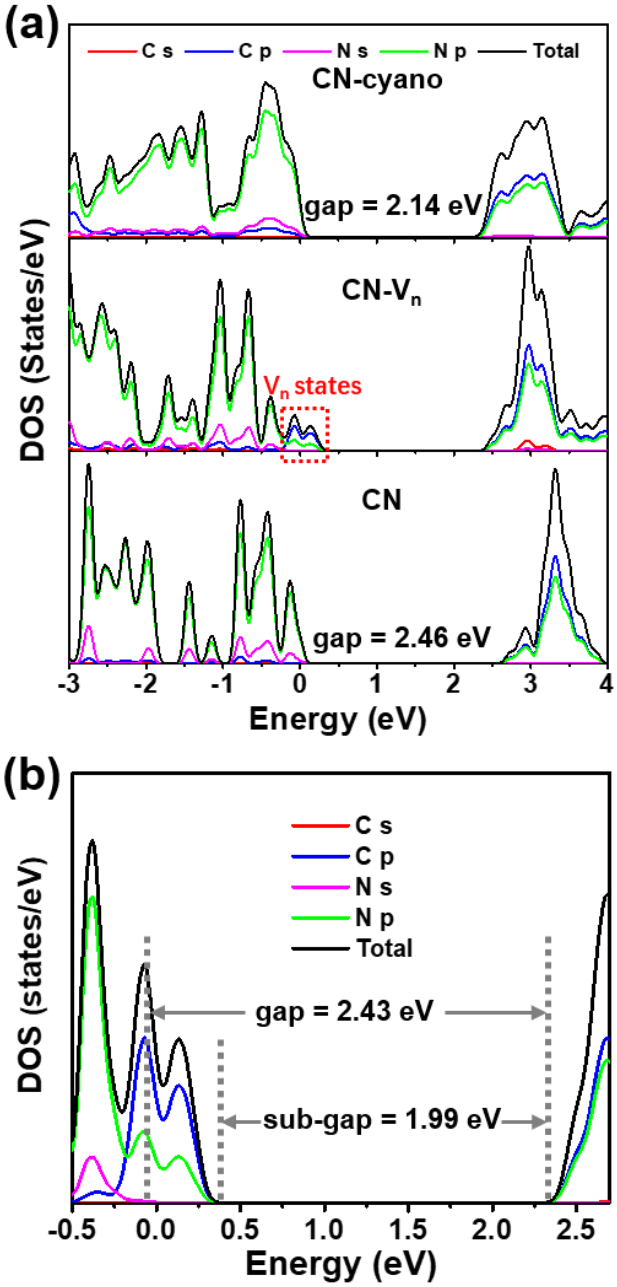

Figure 4. (a) DOS for CN, CN with one V_n, and CN with one cyano group. (b) Enlarged view of the DOS for CN-V_n in the range from −0.5 to 2.75 eV. The E_F is set at 0 eV.

Upon recognizing the change in the optical and electronic properties caused by N defects, we are now in a position to assess the efficacy of DCN for the photocatalytic H_2 evolution. Since DCN absorbs much more visible light than CN, it is supposed that DCN should show much higher activity in the visible-light region. However, the H_2 evolution rate for DCN increases by only ~80% compared with CN (from 1.5 to 2.7 mmol h^{-1}, Figure 5a) under visible-light irradiation ($\lambda > 420$ nm). Deducting the H_2 evolution rate of 0.7 mmol h^{-1} in the region of $\lambda > 460$ nm, DCN shows a more limited enhancement of H_2 evolution compared with CN in the region where both CN and DCN are photocatalytically reactive (420–460 nm). In addition, Figure 5b shows that at a wavelength of 420 nm, the AQE for DCN is lower than that for CN although the absorption of DCN is stronger than that of CN at this wavelength. It turns out that there are some negative factors in DCN competing with the enhanced light absorption, resulting in a limited enhancement of H_2 evolution in the visible-light region. A question naturally arises here: What are the negative factors that limit the photocatalytic activity of DCN? We first examine the possibility of the decreased reduction driving force for H_2 evolution. According to Figure 3d, the introduction of N defects shifts the CBM of DCN down by 0.40 eV but still higher than the H^+/H_2 reduction potential,[9] indicating a decreased reduction driving force. On the other hand, if we consider the fact that the introduction of cyano groups does not change the VBM, the oxidation driving force should be maintained. However, Wu et al. reported that cyano groups could greatly reduce the photooxidation performance.[34] Therefore, another negative factor besides the decreased driving force does exist to limit the photocatalytic activity of DCN. We then consider the possibility of the decreased surface area. However, previous reports have pointed out that the surface area may govern the photocatalytic degradation reactions but it is not the decisive factor for water splitting activities, since for the uphill reaction of water splitting an efficient charge transfer is more urgently required.[10,35] Therefore, we finally investigate the charge transfer by DFT calculations.

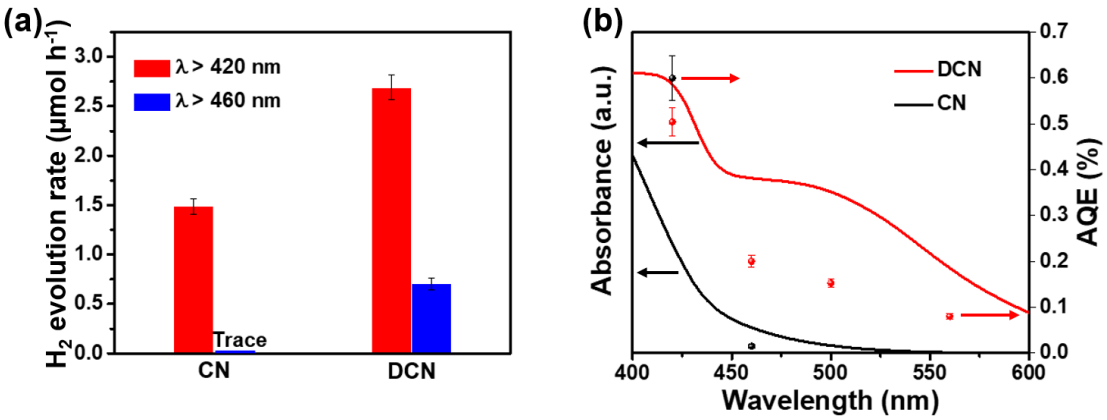

Figure 5. (a) Photocatalytic H_2 evolution under light with $\lambda > 420$ nm and $\lambda > 460$ nm irradiation and (b) wavelength-dependent AQEs for H_2 evolution over CN and DCN.

The charge transfer rate can be evaluated using eqn (1):

$$v = \hbar k/m^* \quad (1)$$

where v is the transfer rate of photogenerated electrons and holes, $\hbar$ is the reduced Planck constant, k is the wave vector, and m^* is the effective mass of the charge carrier. Therefore, smaller m^* results in larger v. Because the photogenerated electrons and holes relax thermally at the bottom of the CB and on top of the VB, respectively, the effective masses of electron (m_e^*) and hole (m_h^*) were estimated by fitting parabolic functions around the CBM and the VBM according to eqn (2):

$$m^* = \hbar^2[\frac{\partial^2 \varepsilon(k)}{\partial k^2}]^{-1} \quad (2)$$

where $\varepsilon(k)$ are the band edge eigenvalues. The calculated m_e^* and m_h^* for CN, CN with one V_n, and CN with one cyano are summarized in Table 2. It can be seen that for CN, m_e^* ($0.47m_0$, m_0 is the mass of free electrons) is smaller than m_h^* ($39m_0$), similar to the previous report.[36] Introduction of N defects, especially the cyano groups leads to larger m_e^* ($0.69m_0$ for V_n and $1.0m_0$ for cyano groups). Such heavier electrons in the CB exhibit slower mobility, inhibiting the ET and thereby resulting in the limited activity for H_2 evolution.

Table 2. The effective masses of electron (m_e*) and hole (m_h*) for CN, CN-V_n, and CN-cyano obtained from DFT calculations. m_0 is the mass of free electron.

Species	CN	CN-V_n	CN-cyano
m_e*/m_0	0.47	0.69	1.0
m_h*/m_0	39	2.2	199

4. Conclusion

In summary, we have shown that the introduction of N defects significantly extends the light-harvesting range of CN by tailing the VB (induced by V_ns) and narrowing the intrinsic bandgap (induced by cyano groups). However, such a wide light-harvesting range does not result in a much enhanced photocatalytic H_2 evolution under visible-light irradiation. The N defects, especially the cyano groups inhibit the ET by increasing the effective mass, which is along with the reduced driving force for H_2 evolution. These factors seriously restrict the photocatalytic activity for H_2 evolution.

It should be noted here that previous reports have also shown that CN with only V_ns exhibits a pronounced enhancement in photocatalytic H_2 evolution under visible-light irradiation.[10,12,15] This is because, in most cases, V_ns are introduced into CN by a post-thermal treatment, probably in the reducing atmosphere. The as-obtained V_ns are mainly located on the surface and serve as highly active sites for H_2 evolution.[10] However, in the present work, N defects are in situ produced during the thermal polymerization process and characterized by bulk properties. And we focus on the fundamental understanding of the effects of the coexistence of V_ns and cyano groups on the photocatalytic H_2 evolution. Regardless of the synthesis method, to extend the light responsive range of a given photocatalyst by doping (or self-doping), band tail states must be formed instead of localized mid-gap states.[37] More importantly, the dispersion degree of the band structure around the CBM and VBM must be maintained to preserve the mobility of charge carriers, maximizing the photocatalytic efficiency in the whole light responsive range.

5. References

1. X. Wang, K. Maeda, A. Thomas, K. Takanabe, G. Xin, J. M. Carlsson, K. Domen and M. Antonietti, *Nat. Mater.*, **2009**, 8, 76–80.
2. Y. Wang, X. Wang and M. Antonietti, *Angew. Chem., Int. Ed.*, **2012**, 51, 68–89.
3. G. Liu, P. Niu, C. Sun, S. C. Smith, Z. Chen, G. Q. Lu and H. M. Cheng, *J. Am. Chem. Soc.*, **2010**, 132, 11642–11648.
4. G. Zhang, M. Zhang, X. Ye, X. Qiu, S. Lin and X. Wang, *Adv. Mater.*, **2014**, 26, 805–809.
5. S. Guo, Z. Deng, M. Li, B. Jiang, C. Tian, Q. Pan and H. Fu, *Angew. Chem., Int. Ed.*, **2016**, 55, 1830–1834.
6. P. Wu, J. Wang, J. Zhao, L. Guo and F. E. Osterloh, *J. Mater. Chem. A*, **2014**, 2, 20338–20344.
7. D. Gao, Q. Xu, J. Zhang, Z. Yang, M. Si, Z. Yan and D. Xue, *Nanoscale*, **2014**, 6, 2577–2581.
8. P. Niu, L. C. Yin, Y. Q. Yang, G. Liu and H. M. Cheng, *Adv. Mater.*, **2014**, 26, 8046–8052.
9. Y. Kang, Y. Yang, L. C. Ying, X. Kang, G. Liu and H. M. Cheng, *Adv. Mater.*, **2015**, 27, 4572–4577.
10. X. Li, G. Hartley, A. J. Ward, P. A. Young, A. F. Masters and T. Maschmeyer, *J. Phys. Chem. C*, **2015**, 119, 14938–14946.
11. Q. Tay, P. Kanhere, C. F. Ng, S. Chen, S. Chakraborty, A. C. H. Huan, T. C. Sum, R. Ahuja and Z. Chen, *Chem. Mater.*, **2015**, 27, 4930–4933.
12. W. Tu, Y. Xu, J. Wang, B. Zhang, T. Zhou, S. Yin, S. Wu, C. Li, Y. Huang, Y. Zhou, Z. Zou, J. Robertson, M. Kraft and R. Xu, *ACS Sustainable Chem. Eng.*, **2017**, 5, 7260–7268.
13. Q. Han, Z. Cheng, B. Wang, H. Zhang and L. Qu, *ACS Nano*, **2018**, 12, 5221–5227.
14. Z. Mo, H. Xu, Z. Chen, X. She, Y. Song, J. Wu, P. Yan, L. Xi, Y. Lei, S. Yuan and H. Li, *Appl. Catal., B*, **2018**, 225, 154–161.

15. P. Niu, H. Li, Y. Ma and T. Zhai, *J. Phys. Chem. C*, **2018**, 122, 20717–20726.
16. Y. Zhang, S. Zong, C. Cheng, J. Shi, P. Guo, X. Guan, B. Luo, S. Shen and L. Guo, *Appl. Catal., B*, **2018**, 233, 80–87.
17. G. Liu, G. Zhao, W. Zhou, Y. Liu, H. Pang, H. Zhang, D. Hao, X. Meng, P. Li, T. Kako and J. Ye, *Adv. Funct. Mater.*, **2016**, 26, 6822–6829.
18. H. Yu, R. Shi, Y. Zhao, T. Bian, Y. Zhao, C. Zhou, G. I. N. Waterhouse, L. Z. Wu, C. H. Tung and T. Zhang, *Adv. Mater.*, **2017**, 29, 1605148.
19. G. Ge, X. Guo, C. Song and Z. Zhao, *ACS Appl. Mater. Interfaces*, **2018**, 10, 18746–18753.
20. Y. Jiang, Z. Sun, C. Tang, Y. Zhou, L. Zeng and L. Huang, *Appl. Catal., B*, **2019**, 240, 30–38.
21. J. Liu, W. Fang, Z. Wei, Z. Qin, Z. Jiang and W. Shangguan, *Appl. Catal., B*, **2018**, 238, 465–470.
22. P. Niu, M. Qiao, Y. Li, L. Huang and T. Zhai, *Nano Energy*, **2018**, 44, 73–81.
23. J. Yuan, X. Liu, Y. Tang, Y. Zeng, L. Wang, S. Zhang, T. Cai, Y. Liu, S. Luo, Y. Pei and C. Liu, *Appl. Catal., B*, **2018**, 237, 24–31.
24. D. Zhang, Y. Guo and Z. Zhao, *Appl. Catal., B*, **2018**, 226, 1–9.
25. F. Yang, D. Liu, Y. Li, L. Cheng and J. Ye, *Appl. Catal., B*, **2019**, 240, 64–71.
26. J. Tang, J. R. Durrant and D. R. Klug, *J. Am. Chem. Soc.*, **2008**, 130, 13885–13891.
27. P. Niu, G. Liu and H. M. Cheng, *J. Phys. Chem. C*, **2012**, 116, 11013–11018.
28. D. Zhang, X. Han, T. Dong, X. Guo, C. Song and Z. Zhao, *J. Catal.*, **2018**, 366, 237–244.
29. J. Yu, J. Low, W. Xiao, P. Zhou and M. Jaroniec, *J. Am. Chem. Soc.*, **2014**, 136, 8839−8842.
30. S. Grimme, *J. Comput. Chem.*, **2006**, 27, 1787−1799.
31. H. Gao, S. Yan, J. Wang, Y. A. Huang, P. Wang, Z. Li and Z. Zou, *Phys. Chem. Chem. Phys.*, **2013**, 15, 18077–18084.
32. Y. Li, H. Xu, S. Ouyang, D. Lu, X. Wang, D. Wang and J. Ye, *J. Mater. Chem. A*, **2016**, 4, 2943–2950.

33. X. Chen, L. Liu, P. Y. Yu and S. S. Mao, *Science*, **2011**, 331, 746–750.
34. W. Wu, J. Zhang, W. Fan, Z. Li, L. Wang, X. Li, Y. Wang, R. Wang, J. Zheng, M. Wu and H. Zeng, *ACS Catal.*, **2016**, 6, 3365–3371.
35. X. Li, A. F. Masters and T. Maschmeyer, *ChemCatChem*, **2014**, 7, 121–126.
36. W. Yu, J. Chen, T. Shang, L. Chen, L. Gu and T. Peng, *Appl. Catal., B*, **2017**, 219, 693–704.
37. S. K. Cushing, F. Meng, J. Zhang, B. Ding, C. K. Chen, C. J. Chen, R. S. Liu, A. D. Bristow, J. Bright, P. Zheng and N. Wu, *ACS Catal.*, **2017**, 7, 1742–1748.

Chapter 3. Shallow Trap State-Induced Efficient Electron Transfer at the Interface of Heterojunction Photocatalysts: The Crucial Role of Vacancy Defects

1. Introduction

Solar light-driven H_2 production from water using semiconductor photocatalysts holds great potential in fulfilling the challenge of a green and sustainable energy economy.[1] However, currently, the practical application of photocatalysis is still thwarted by the low conversion efficiency due to fast charge recombination and insufficient reaction sites in photocatalysts.[2] Integrating a second semiconductor to form a heterojunction architecture has been proved to be one of the most promising ways for resolving these problems.[3] Among various heterojunctions, the type-II junction is generally favored and widely studied, because the mutually staggered band levels drive photogenerated charges to transfer across the interface, resulting in the spatial separation of electrons and holes.[3] Accordingly, the performance of a given heterojunction photocatalyst for H_2 evolution strongly depends on the ET efficiency at the interface which is determined by the electronic structure of each component apart from the interaction degree.[3]

On the other hand, it is well documented that constructing defects, especially vacancies, is an effective strategy to modulate the electronic structures of semiconductor photocatalysts.[4] This inspires us to consider its potential roles in the IET of heterojunctions. In this regard, previous reports have shown that vacancies in the photogenerated electron-acceptor side of a heterojunction serve as electron-trapping sites to promote the IET.[5,6] In contrast, how vacancies in the electron-donor side influence the IET has not been clarified due to a lack of a detail study of ET kinetics, which has obviously hindered the comprehensive understanding of the structure−property relationship of defect-related heterojunction photocatalysts.

Given that the two-dimensional (2D) structure of nanosheets can readily shorten the diffusion length of photogenerated electrons to suppress the bulk charge

recombination,[7] and nanodots can promote the IET,[8] we take CN nanosheets/MS nanodots as heterojunction photocatalyst prototypes. By the aid of DFT calculations and fs-TDRS, we study the aspects about the vacancy-involved electronic structure and ET kinetics at the heterojunction interface which have not been fully understood before. Our study reveals that vacancy defects can induce electronic effects that modify the IET kinetics to efficiently drive photocatalytic H_2 evolution, and thereby providing a powerful tool to design and optimize ET reactions for photocatalysis.

2. Experimental Section

Preparation of CN with and without V_n defects (CN-V_n and CN). CN-V_n and CN were synthesized via a thermal polymerization method described in the previous paper.[9] In detail, dicyandiamide (6 g) in a covered crucible was calcined at 550 or 600 °C in a muffle furnace for 4 h using a heating rate of 2 °C min^{-1}. Heating at 550 and 600 °C produced a yellow CN and an orange CN-V_n, respectively. No other defects such as cyano groups were introduced. Then, the agglomerates were grounded into powder. Second, to exfoliate bulk CN-V_n and CN into nanosheets, 0.4 g of the as-obtained powder was uniformly dispersed into an alumina ark with dimensions of 50 × 30 × 10 mm to make sufficient contact with air, and again heated at 520 °C for 4 h with a heating rate of 2 °C min^{-1}.

Preparation of CN/MS and CN-V_n/MS. CN/MS and CN-V_n/MS were synthesized by an in situ photodeposition method.[10] Typically, 20 mg of CN (CN-V_n) was dissolved into a mixture of de-ionized (DI) water (8 mL) and lactic acid (2 mL). Then, 1 mL of 1 mg mL^{-1} $(NH_4)_2MoS_4$ water solution was added into the mixture. The solution was irradiated under a UV-LED source (Asahi Spectra, POT-365, 100 mW cm^{-2}) with the de-aeration with N_2 for 1 h. The product was centrifuged, washed three times by water and ethanol, and dried under 60 °C.

Characterization. The samples were characterized by XRD, TEM, XPS, and UV−vis DRS as in Chapter 1. Atomic force microscopy (AFM) was performed using a Seiko Instruments (Chiba, Japan) SPI3800/SPA400 AFM with a tapping mode under ambient

conditions. The contents of Mo and S were determined by an inductively coupled plasma (ICP) emission spectrometer (Shimadzu, ICPS-8100).

Photocatalytic H_2 evolution. The photocatalytic H_2 evolution reaction was carried out like Chapter 2 except that (i) lactic acid was used as the sacrificial agent and (ii) cocatalyst, Pt, was not used.

DFT calculation. All calculations were performed like Chapter 2 except that (i) a vacuum space of 15 Å was used to separate the interactions between neighboring slabs, (ii) the energy convergence tolerance was set to be 1.0×10^{-5} eV per atom, and (iii) No scissor operator was applied.

Fs-TDRS measurement. The fs-TDRS were measured by the pump and probe method using a regeneratively amplified titanium sapphire laser (Spectra-Physics, Spitfire Pro F, 1 kHz) pumped by a Nd:YLF laser (Spectra-Physics, Empower 15). The seed pulse was generated by a titanium sapphire laser (Spectra-Physics, Mai Tai VFSJW; FWHM 80 fs). The output (420/600 nm, 3 μJ per pulse) of the optical parametric amplifier (Spectra-Physics, OPA-800CF-1) was used as the excitation pulse. A white light continuum pulse, which was generated by focusing the residual of the fundamental light on a sapphire crystal after the computer controlled optical delay, was divided into two parts and used as the probe and the reference lights, of which the latter was used to compensate for the laser fluctuation. Both probe and reference lights were directed to the sample powder coated on the glass substrate, and the reflected lights were detected by a linear InGaAs array detector equipped with the polychromator (Solar, MS3504). The pump pulse was chopped with a mechanical chopper synchronized to one-half of the laser repetition rate, resulting in a pair of spectra with and without the pump. The transient absorption (TA) signal of the TDR measurements is presented as percentage absorption, % Abs = $100(1 - R/R_0)$, where R and R_0 are the intensities of the diffuse reflected light with and without pump, respectively, because the % Abs is proportional to the concentration of transient species within the experimental error for % Abs values below 20% in the present measurement. Therefore, in the manuscript TDR spectra are interchanged with the term TA spectra. All measurements were carried out at room

temperature.

3. Results and Discussion

The existence of V_n defects was confirmed by using XRD, EA, and XPS like Chapter 2. Briefly, the N/C atomic ratio of CN-V_n (1.50) is smaller than that of CN (1.53), indicating the presence of V_ns. The N_{2C}/N_{3C} atomic ratio drops from 1.64 to 1.27 once V_ns are introduced, demonstrating that V_ns are preferentially engineered at the N_{2C} site. As observed by TEM and AFM, both CN (Figure 1) and CN-V_n (Figure 2) present a similar 2D sheet-like morphology, with an ultrathin thickness of ~1.4 nm. When loading MoS_2 nanodots, the morphology of CN-V_n remains unchanged (Figure 3a). The HRTEM image of CN-V_n (Figure 3a) clearly shows that the MS nanodots are successfully deposited on the surface of CN-V_n with a lattice spacing of 0.27 nm, corresponding to the (100) crystal plane of MS.[10] The weight percentages of Mo and S in CN/MS are very close to those in CN-V_n/MS as confirmed by ICP analysis (Table 1). The atomic ratio of Mo to S is smaller than the stoichiometric value of 0.5 due to the existence of unsaturated S atoms on the edge. Taken together, we clearly conclude that the CN-V_n/MS heterojunction with interfacial vacancies has been successfully fabricated, thereby providing an ideal model to investigate the role of interfacial vacancies in photocatalytic H_2 evolution, as schematically illustrated in Figure 3b.

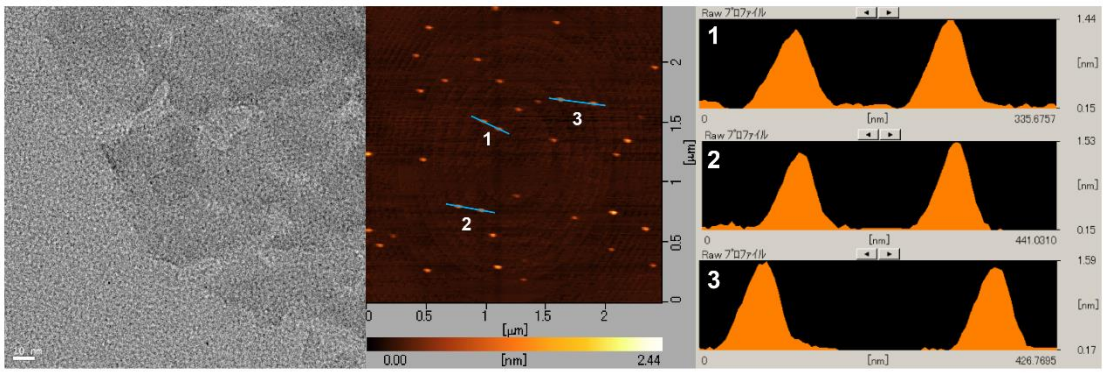

Figure 1. TEM (left) and AFM (middle and right) images of CN. The scale bar in the TEM image is 10 nm.

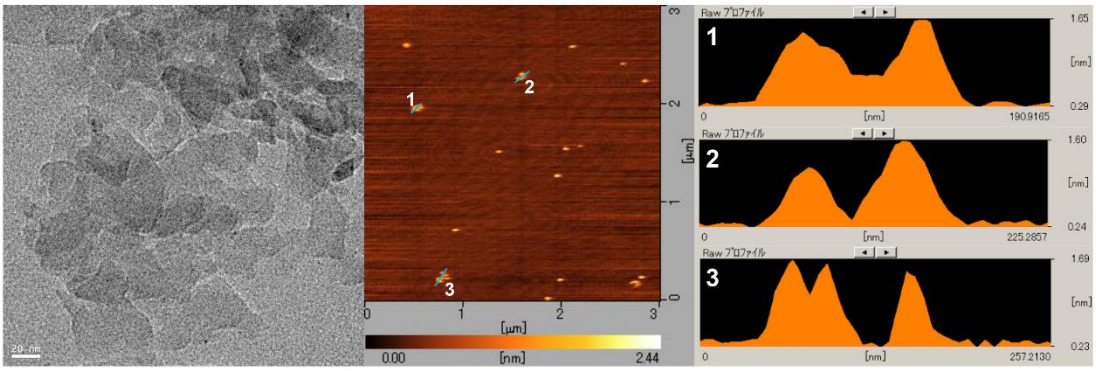

Figure 2. TEM (left) and AFM (middle and right) images of CN-V_n. The scale bar in the TEM image is 20 nm.

Table 1. Weight percentages of Mo and S in CN/MS and CN-V_n/MS determined by ICP.

Sample	Mo (wt.%)	S (wt.%)	Mo/S (at.)
CN/MS	0.80	0.67	0.42
CN-V_n/MS	0.77	0.65	0.40

It is well known that the introduction of V_ns can modify the optical properties of CN. As evidenced by UV−vis DRS (Figure 3c), CN has an absorption edge at ~425 nm, corresponding to a bandgap of ~2.92 eV which is larger than the typical bandgap of ~2.7 eV for the bulk CN due to the quantum confinement effect.[11] As compared to CN, CN-V_n shows a Urbach tail absorption in the region of 425−600 nm, which is usually attributed to the shallow mid-gap states overlapping with the energy band edge.[12,13] In addition, the light absorption of CN-V_n in the region of 600 nm−NIR is also slightly enhanced, similar to the previous report.[14] On the other hand, the addition of MS nanodots significantly enhances the light absorption of CN and CN-V_n in the whole region of 425 nm−NIR due to the intrinsic background absorption of black or dark colored MS.[8,10] Figure 3d compares the photocatalytic H_2 evolution activities of as-prepared samples. Neither CN nor CN-V_n shows H_2 production activity under visible-light irradiation ($\lambda > 420$ nm). As expected, loading MS makes both CN and CN-V_n active, and, notably, the H_2 evolution over CN-V_n/MS is nearly three times as fast as that over CN/MS. Given that the bare MS is inactive,[15] the activity of CN/MS (CN-

V_n/MS) is attributed to the transfer of photogenerated electrons from CN (CN-V_n) to the reactive sites in MS (unsaturated bridging S_2^{2-} and apical S^{2-}).[8,16] According to the S 2p XPS results (Figure 4), difference in the atomic percentages of unsaturated bridging S_2^{2-} and apical S^{2-} in CN and CN-V_n is small (44.3% *vs.* 49.0%). Therefore, the improved photocatalytic performance mentioned above can be attributed to the enhanced light absorption (Figure 3c) as well as the likely more efficient IET in the presence of V_ns. In the following, we investigate the V_n-mediated IET to test this prediction.

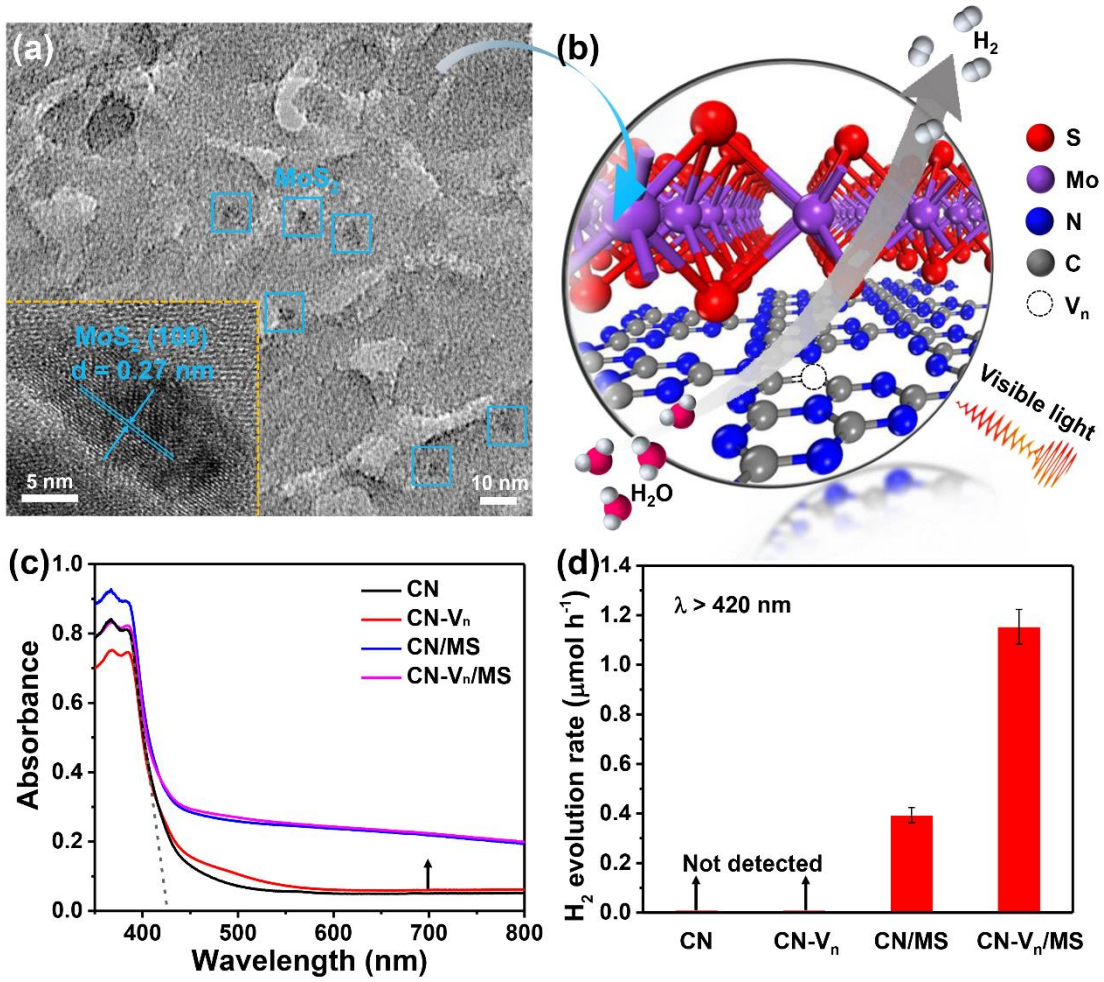

Figure 3. (a) HRTEM image of CN-V_n/MS. (b) A schematic illustration of CN-V_n/MS with interfacial V_ns for photocatalytic H_2 evolution. (c) UV−vis DRS. The arrow indicates the slightly enhanced absorption of CN-V_n in the region of 600 nm–NIR. (d) Photocatalytic H_2 evolution rates.

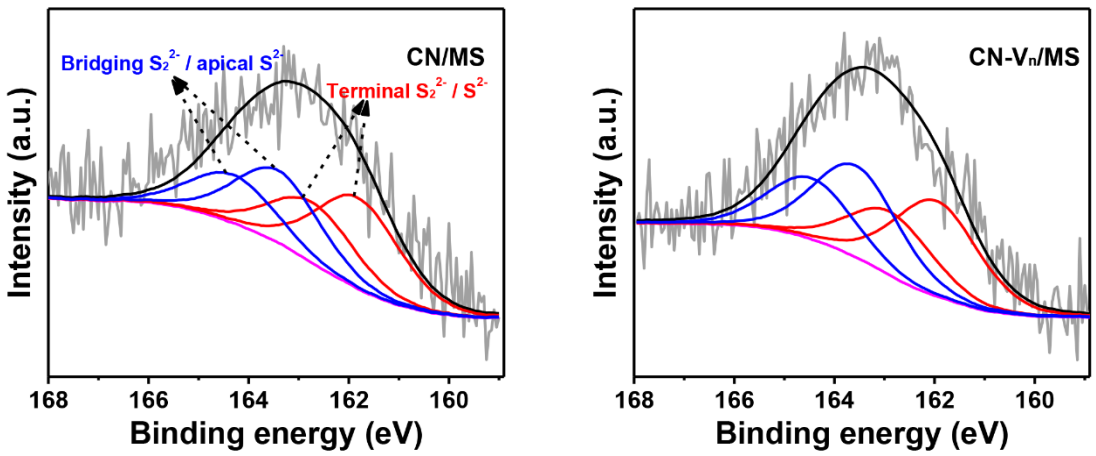

Figure 4. S 2p XPS spectra of CN/MS and CN-V_n/MS.

In general, the interfacial charge transfer in a given heterojunction photocatalyst strongly depends on the electronic structure of the individual component. Herein, we carried out DFT calculations to decode the role of V_ns in the electronic structure of CN-V_n/MS. For a start, we calculated the DOS of a CN monolayer. As shown in Figure 5a, the bandgap of CN is calculated to be ~1.2 eV, which is smaller than the experimental value in this work, due to the well-known underestimation of the bandgap by the GGA method.[12,17] The root of such underestimation is the delocalization error of approximate functionals.[18] However, it does not prevent us from qualitatively analyzing the electronic structure.[12,17] The CBM of CN mainly consists of C 2p and N 2p orbitals, while the VBM is dominated by N 2p orbital, consistent with the previous report.[19] Once a N_{2C} vacancy is introduced, two groups of continuum mid-gap states (V_n states) with the Fermi level in between can be observed, herein denoted $C^{3+}(V_n)$ and $C^{4+}(V_n)$ depending on their occupation. It should be mentioned that the calculation results here are different from those in Chapter 2. This is because the model used here is monolayer while that in Chapter 2 is bulk. Moreover, the defect concentration is also different. Similar results are reported for TiO_2 with V_os, where occupied and unoccupied V_o states are found in the forbidden band of TiO_2.[20] Therefore, the physical nature of $C^{3+}(V_n)$ and $C^{4+}(V_n)$ states can be understood in analogy to the case of V_os.[21,22] That is, the loss of N atoms (formation of V_ns) leaves excess electrons, which can transfer to the adjacent C atoms (generating $C^{3+}(V_n)$ states), or C atoms far away in the stoichiometric

framework, being thermally excited to the CB (generating C^{3+}(CB) states) and thereby leaving unoccupied $C^{4+}(V_n)$ states. The thermally excited electrons in the CB result in n-type conductivity, and is in favor of the CS and transport.[22] Moreover, thermal excitation to the CB can only be possible for the electrons in vacancy states close to the band edge, meaning that $C^{4+}(V_n)$ states should locate just below the CB (in the form of shallow states). On the other hand, the $C^{3+}(V_n)$ states are occupied, indicating that they are too far from the CB (in the form of deep states) for thermal excitation. Therefore, electronic transition from VB to $C^{4+}(V_n)$ states and that from $C^{3+}(V_n)$ states to $C^{4+}(V_n)$ states or CB are responsible for the Urbach tail and 600 nm–NIR absorption of CN-V_n, respectively, as shown in Figure 5b. In addition, the Urbach tail absorption is much stronger than the 600 nm – NIR absorption, indicating that $C^{4+}(V_n)$ states dominate the V_n states in this work. The position of the Urbach tail can be estimated by plotting the absorption edge data using eqn (1) originally given by Urbach:[23]

$$a = a_0 \exp(hv/Eu) \quad (1)$$

where a is the absorption coefficient, a_0 is a constant, hv is the incident photon energy, and Eu is the energy of the band tail (Urbach energy, herein calculated to be ~0.7 eV).

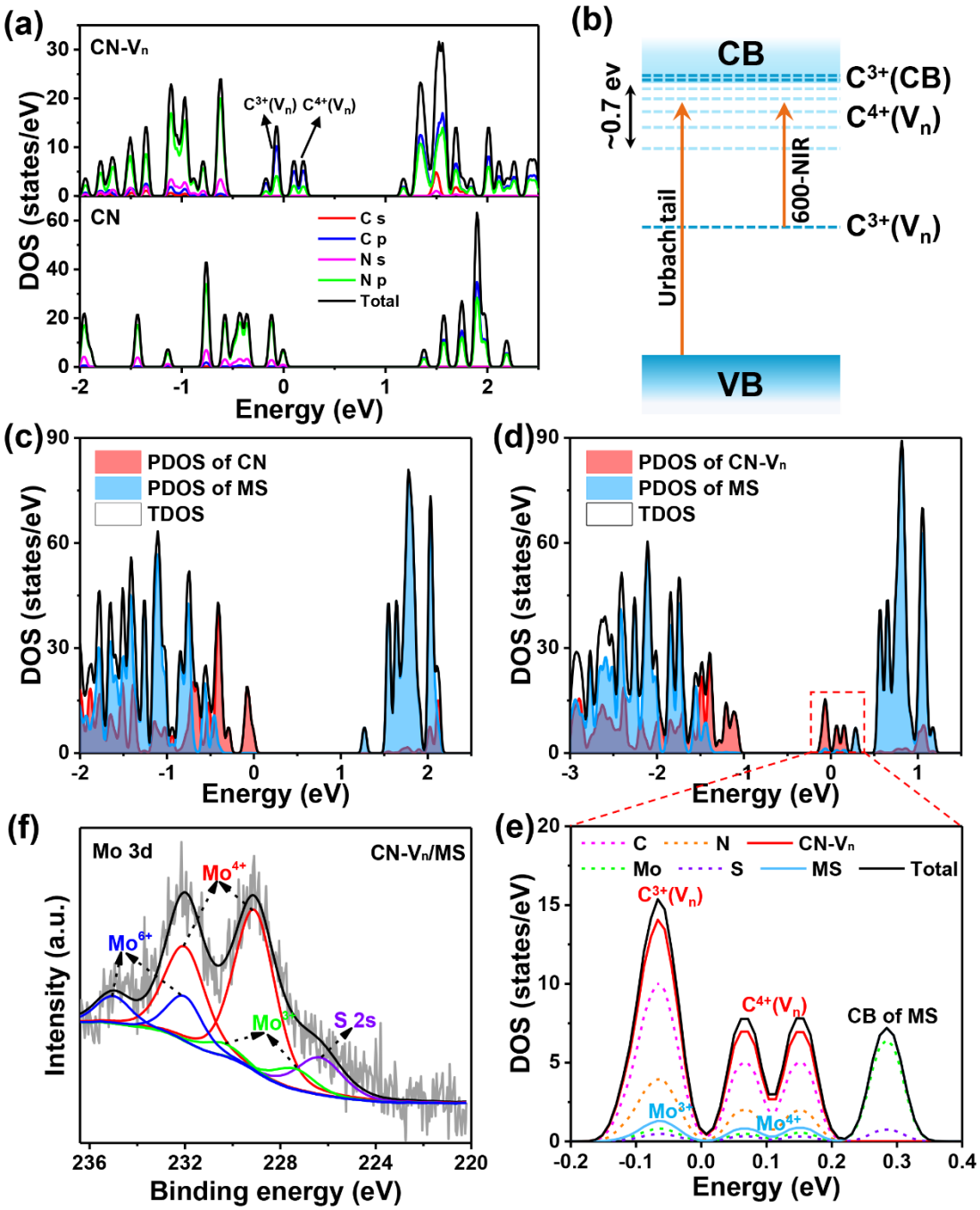

Figure 5. (a) Calculated DOS of CN and CN-V_n. (b) A schematic illustration of the electronic structure of CN-V_n. The dark and light dash lines represent occupied and unoccupied states, respectively. Calculated total DOS (TDOS) and partial DOS (PDOS) of (c) CN/MS and (d) CN-V_n/MS. (e) Enlarged view of the DOS in (d). The E_F is set at 0 eV for (a, c, d, and e). (f) Mo 3d XPS spectrum of CN-V_n/MS.

When coupled with a MS monolayer (simulation of CN/MS), no mid-gap states can be observed in the calculated DOS (Figure 5c). It indicates that the interlayered

interaction between CN and MS is weak due to the absence of covalent bonding at the interface. Moreover, the CBM of CN is higher than that of MS, whereas the VBM of MS is lower than that of CN, presenting a typical type-II band alignment structure. Unexpectedly, in the case of CN-V_n/MS, it can be found that besides the V_n states, an occupied state (Mo^{3+} state) corresponding to the ET from C 2p to Mo 4d orbitals (Figures 5d and e) is formed, that is, the excess electrons trapped at C^{3+} atom sites can partially transfer to Mo atom sites. Similar to the case of C^{3+} states, the Mo^{3+} states are accompanied by shallow Mo^{4+} states due to the thermal excitation to CB. Such IET induced by vacancy states is characteristic of a stronger interlayered interaction as is usually observed for V_o-defective metal oxide/noble metal hybrid photocatalyst systems,[24–26] and has recently been described for CN-V_n/Au system.[27] Herein, we successfully extend it to CN-V_n/non-noble metal system. In addition to the theoretical evidence, the IET can be further confirmed by the experimental results as in Mo 3d XPS (Figure 5f). We can find a pair of additional peaks centered at 227.4 and 230.4 eV corresponding to Mo $3d_{5/2}$ and Mo $3d_{3/2}$ peaks of Mo^{3+} species,[28] respectively, in CN-V_n/MS, indicating the electron donation from C atoms. It has been reported that the CBMs of CN and MS nanosheet are at ~−1.0[29] and ~−0.1 eV[30] *vs.* Normal Hydrogen Electrode (NHE), respectively, and V_ns have negligible effect on the intrinsic energy band position of CN. Consequently, a simplified schematic illustration for the electronic structure of CN-V_n/MS is shown in Figure 6.

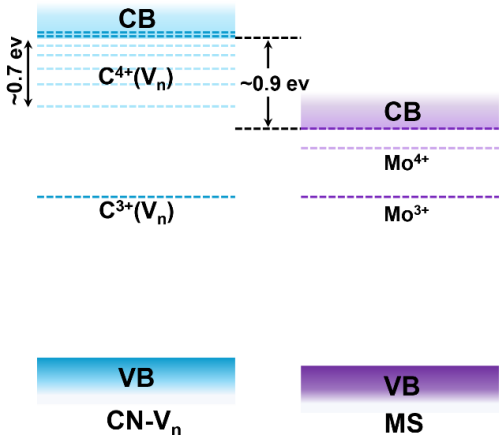

Figure 6. A schematic illustration of the electronic structure of CN-V_n/MS. The dark and light dash lines represent occupied and unoccupied states, respectively.

We now turn to investigate how the electronic structure determines the photogenerated ET at the interface of CN/MS (CN-V_n/MS), by means of fs-TDRS, a powerful tool for tracking the relaxation kinetics of charge carriers in photocatalyst systems in real time. We present a representative set of data observed at 950 nm in Figure 7. Quantitative information on the electron kinetics is reported in Tables 2 and 3, which is obtained by fitting the decay traces with a multiexponential eqn (2):[31,32]

$$\%\mathrm{Abs} = A_0 + \sum_i A_i \exp(-t/\tau_i) \quad (2)$$

where τ_i is the lifetime and A_i is the weighted coefficient assuming a long-lived component (τ_0 >> 1 ns) as a constant (A_0). The smallest number of τ_i, which resulted in the R^2 closest to 1, was used for each fit.

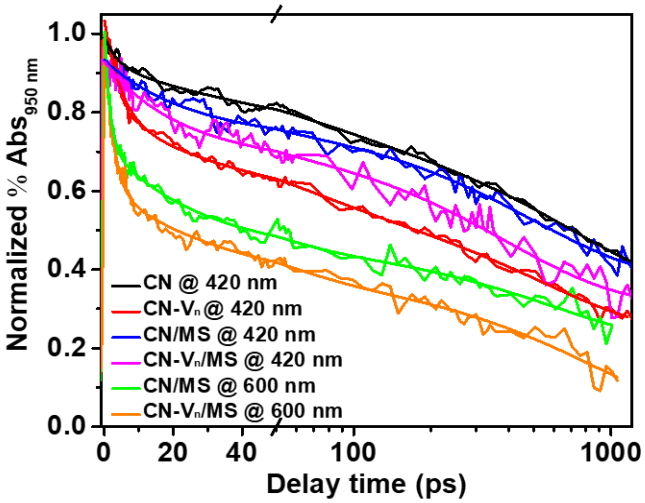

Figure 7. Normalized TA traces probed at 950 nm during 420/600 nm laser flash photolysis.

Table 2. Weighted coefficients of the TA Decay.

Sample[a]	A_0	A_1	A_2	A_3
CN (420 nm)	0.34	0.07	0.15	0.44
CN-V_n (420 nm)	0.24	0.24	0.20	0.35
CN/MS (600 nm)	0.21	0.29	0.25	0.26
CN-V_n/MS (600 nm)	0.02	0.38	0.22	0.37
CN/MS (420 nm)	0.38		0.15	0.41
CN-V_n/MS (420 nm)	0.31		0.19	0.43

Table 3. Lifetimes of the TA Decay.

Sample[a]	τ_0 **(ns)**	τ_1 **(ps)**	τ_2 **(ps)**	k_2 **(10^{10} s^{-1})**[b]	τ_3 **(ps)**	k_3 **(10^8 s^{-1})**[b]
CN (420 nm)	≫1	3.8	58		710	
CN-V_n (420 nm)	≫1	4.8	48		530	
CN/MS (600 nm)	≫1	1.6	27		610	
CN-V_n/MS (600 nm)	≫1	2.4	35		860	
CN/MS (420 nm)	≫1		20	3.3	500	5.9
CN-V_n/MS (420 nm)	≫1		18	3.5	390	6.8

[a]The numbers in parentheses are excitation wavelengths. [b]IET rate constant, $k_i = 1/\tau_i$ (CN/MS or CN-V_n/MS) − $1/\tau_i$ (CN or CN-V_n).[2]

Upon excitation at 420 nm, the photogenerated electrons in bare CN exhibit short lifetimes of τ_1 = 3.8 ps (7%), τ_2 = 58 ps (15%) and τ_3 = 710 ps (44%), and a long lifetime of τ_0 >> 1 ns (34%). As schematically illustrated in Figure 8a, the short lifetimes are attributed to the relaxation to STSs with different depths (denoted STS_1, STS_2, and STS_3), while the long lifetime is assigned to the relaxation to the deep trap state

(denoted DTS) and subsequent recombination,[2,32–34] given that the deeply trapped electrons in CN have lifetimes of micro- to milli-second scale observed by microsecond-TA spectroscopy.[35] The DTS is reported to locate at energy of 1 eV or more below the CBM of CN, which is lower than the H^+/H_2 reduction potential.[35] For CN-V_n, it can be found that the A_1 increases significantly (from 7% to 24%) and A_2 increases slightly (from 15% to 20%) with respect to those for CN. Since occupied $C^{3+}(V_n)$ states act as hole traps and their proportion in V_n states is small, they do not affect the electron decay kinetics. Therefore, the results above indicate that $C^{4+}(V_n)$ states act as shallow electron TSs and increase the density of STS as the depth decreases, consistent with the characteristic of $C^{4+}(V_n)$ state-induced tail absorption (Figure 5b). In order to study the electron decay kinetics in MS, MS in CN/MS (CN-V_n/MS) was selectively excited by a 600 nm pump laser. Neither bare CN nor CN-V_n showed measurable response under 600 nm pump. Therefore, the TA signal was resulted from the electrons in MS. By comparing A_i and τ_i for CN/MS (CN-V_n/MS), we can draw a similar conclusion to the case of $C^{4+}(V_n)$ states, that is, Mo^{4+} states act as electron TSs and increase the density of STS_1.

Next, we investigated the IET by exciting CN/MS (CN-V_n/MS) at 420 nm. The shortest lifetime, τ_1, is ignored in the fittings due to ultrashort lifetimes. Considering that the content of MS is small, the electrons in CN/MS (CN-V_n/MS) mostly result from the excited CN (CN-V_n). Then, let us turn to compare CN/MS (CN-V_n/MS) with bare CN (CN-V_n) with the 420 nm pump. It can be seen that τ_2 and τ_3 for CN/MS (CN-V_n/MS) are shorter than those for bare CN (CN-V_n). Such a change should be attributed to the opening of an additional decay channel mediated by MS.[2,34] In this particular case, the photogenerated electrons transfer from not only the CB and but also STSs of CN (CN-V_n) to the MS part leading to spatial CS, in competition with being trapped by TSs. The calculated ET rate constants k_2 and k_3 for CN-V_n/MS are larger than those for CN/MS, indicating that a more efficient ET has been achieved in the presence of V_ns.

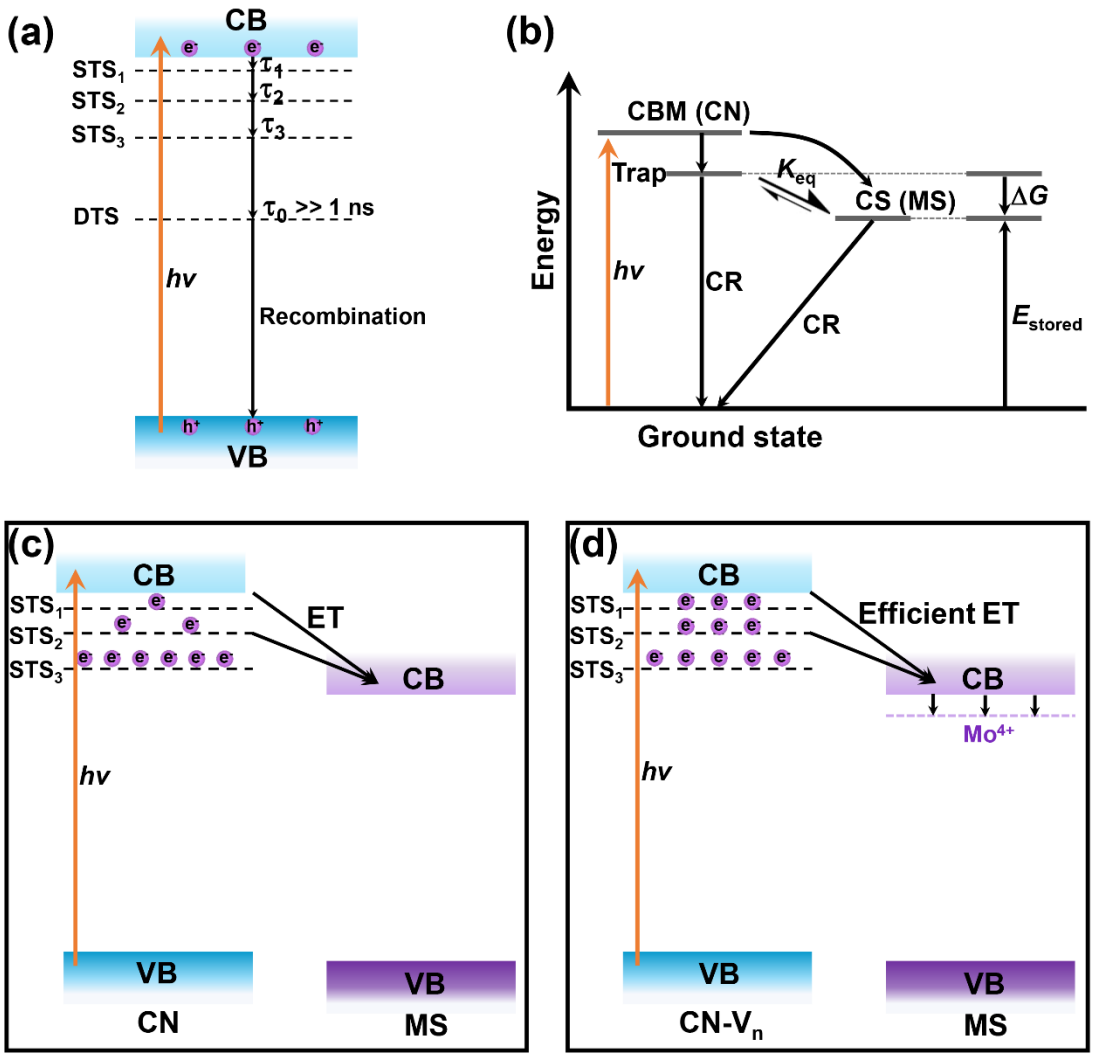

Figure 8. Schematic illustrations of (a) electron relaxation to STSs with different depths (STS_1, STS_2 and STS_3) and DTS, (b) proposed ET model, CS for charge separation, CR for charge recombination and E_{stored} for energy stored, and ET at the interface of (c) CN/MS and (d) CN-V_n/MS. The DTS is not shown in (b–d) because it lies below the CBM of MS, inhibiting ET from CN to MS.

To explain the significant differences in the electron decay kinetics of bare CN (CN-V_n) and CN/MS (CN-V_n/MS), in light of the indications that MS acts as an additional path for ET, we propose a simple transfer model schematically illustrated in Figure 8b, similar to that developed for N-Ta_2O_5/Ru complex system.[36] Upon photoexcitation, the as-generated electrons in the CB of CN decay through trapping into TSs or transfer to the CB of MS to form spatial CS states.[37] We assume that the TSs and CS states are under fast thermal equilibrium, such that the population ratios may be calculated by a

Boltzmann distribution:

$$n_{Trap}/n_{CS} = K_{eq} = \exp(-\Delta G/k_B T) \quad (3)$$

where n_{Trap} and n_{CS} are the population of TSs and CS states, respectively, K_{eq} is the equilibrium constant, k_B is Boltzmann's constant, T is temperature, and ΔG is the energy difference between TSs and CS states. Shallower electron trapping leads to an increase in the energetic difference (ΔG) for electrons in CS states to reach TSs. The thermal equilibrium pushes further to CS (lower K_{eq}), depopulating trapping to generate CS states. As mentioned above, compared to CN, more photogenerated electrons are shallowly trapped (especially in STS_1) in CN-V_n due to the existence of $C^{4+}(V_n)$ states (Figures 8c and d). These electrons possessing high ΔG transfer efficiently to the CB of MS or are subsequently trapped by Mo^{4+} states. As Mo^{4+} states are STSs, electrons in these states have higher mobility to reach the active sites and driving force for the subsequent photocatalytic H_2 evolution than those in the DTS.

Our model provides fundamental guidance in understanding the photocatalytic mechanism of vacancy-deficient heterojunctions. Given that the Urbach tail states are active for H_2 evolution, the enhanced performance should be attributed to the higher light-harvesting capacity as a direct result of the electronic transitions to the unoccupied vacancy states, the more efficient IET induced by the vacancy-generated STSs, as well as the higher mobility and driving force of the transferred electrons in STSs caused by the excess electron donation from the C^{3+} species. The higher N vacancy density of CN can result in the increased proportion of the DTS, in which photogenerated electrons can hardly transfer across the interface. Therefore, there is a trade-off between a favorable improvement in light-harvesting through more unoccupied vacancy states and an unfavorable decrease in IET efficiency through a higher number of DTS. As a result, heterojunction photocatalysts with excessive vacancy defects cannot achieve higher performance for H_2 evolution. However, the photogenerated electrons in the DTS are expected to be utilized when coupled with semiconductors with lower CBMs for reactions with less negative reduction potentials such as pollutant degradations. Based on the insights above, we can see a potential opportunity to fine-tune the IET of

heterojunction photocatalysts by engineering vacancy defects for specific target reactions.

4. Conclusion

In summary, we have provided insights into the role of vacancy defects in the IET of a typical heterojunction photocatalyst (CN/MS). Theoretical simulations show that V_n formation in CN introduces mid-gap states ($C^{3+}(V_n)$ and, predominantly, $C^{4+}(V_n)$ states). When coupled with MS, the excess electrons accompanied by V_ns could partially transfer to MS part to form Mo^{3+} and, predominantly, Mo^{4+} states in the forbidden band of MS, resulting in a strong interaction between CN-V_n and MS. Combined with fs-TDRS results, we find that $C^{4+}(V_n)$ states act as STSs for photogenerated electrons. The resulting high density of STSs facilitates the IET process due to the large energy difference between STSs and CS states. In addition, the transferred photogenerated electrons in MS could be subsequently trapped by shallow Mo^{4+} states, where they possess high mobility and driving force for photocatalytic H_2 evolution. The above findings suggest that engineering of TSs by introducing vacancies has great promise in tuning the IET of heterojunction photocatalysts for a wide range of photocatalytic applications.

5. References

1. Z. Wang, Y. Inoue, T. Hisatomi, R. Ishikawa, Q. Wang, T. Takata, S. Chen, N. Shibata, Y. Ikuhara and K. Domen, *Nat. Catal.*, **2018**, 1, 756−763.
2. W. Bi, L. Zhang, Z. Sun, X. Li, T. Jin, X. Wu, Q. Zhang, Y. Luo, C. Wu and Y. Xie, *ACS Catal.*, **2016**, 6, 4253−4257.
3. J. Low, J. Yu, M. Jaroniec, S. Wageh and A. A. Al-Ghamdi, *Adv. Mater.*, **2017**, 29, 1601694.
4. A. Naldoni, M. Altomare, G. Zoppellaro, N. Liu, Š. Kment, R. Zbořil and P. Schmuki, *ACS Catal.*, **2019**, 9, 345−364.

5. H. Shi, S. Long, S. Hu, J. Hou, W. Ni, C. Song, K. Li, G. G. Gurzadyan and X. Guo, *Appl. Catal., B*, **2019**, 245, 760−769.
6. X. An, L. Zhang, B. Wen, Z. Gu, L.-M. Liu, J. Qu and H. Liu, *Nano Energy*, **2017**, 35, 290−298.
7. X. Jiao, Z. Chen, X. Li, Y. Sun, S. Gao, W. Yan, C. Wang, Q. Zhang, Y. Lin, Y. Luo and Y. Xie, *J. Am. Chem. Soc.*, **2017**, 139, 7586−7594.
8. M.-Q. Yang, C. Han and Y.-J. Xu, *J. Phys. Chem. C*, **2015**, 119, 27234−27246.
9. P. Niu, G. Liu and H.-M. Cheng, *J. Phys. Chem. C*, **2012**, 116, 11013−11018.
10. X. Shi, M. Fujitsuka, S. Kim and T. Majima, *Small*, **2018**, 14, 1703277.
11. P. Niu, L. Zhang, G. Liu and H.-M. Cheng, *Adv. Funct. Mater.*, **2012**, 22, 4763−4770.
12. W. Tu, Y. Xu, J. Wang, B. Zhang, T. Zhou, S. Yin, S. Wu, C. Li, Y. Huang, Y. Zhou, Z. Zou, J. Robertson, M. Kraft and R. Xu, *ACS Sustainable Chem. Eng.*, **2017**, 5, 7260–7268.
13. H. Yaghoubi, Z. Li, Y. Chen, H. T. Ngo, V. R. Bhethanabotla, B. Joseph, S. Ma, R. Schlaf and A. Takshi, *ACS Catal.*, **2015**, 5, 327−335.
14. P. Niu, H. Li, Y. Ma and T. Zhai, *J. Phys. Chem. C*, **2018**, 122, 20717–20726.
15. P. Zhang, T. Tachikawa, M. Tachikawa and T. Majima, *Chem. Commun.*, **2015**, 51, 7187−7190.
16. Y.-H. Chang, C.-T. Lin, T.-Y. Chen, C.-L. Hsu, Y.-H. Lee, W. Zhang, K.-H. Wei and L.-J. Li, *Adv. Mater.*, **2013**, 25, 756−760.
17. J. Zhang, P. Zhou, J. Liu and J. Yu, *Phys. Chem. Chem. Phys.*, **2014**, 16, 20382−20386.
18. A. J. Cohen, P. Mori-Sánchez and W. Yang, *Science*, **2008**, 321, 792−794.
19. J. Liu and E. Hua, *J. Phys. Chem. C*, **2017**, 121, 25827−25835.
20. S. K. Cushing, F. Meng, J. Zhang, B. Ding, C. K. Chen, C. Chen, R. Liu, A. D. Bristow, J. Bright, P. Zheng and N. Wu, *ACS Catal.*, **2017**, 7, 1742–1748.
21. B. Liu, K. Cheng, S. Nie, X. Zhao, H. Yu, J. Yu, A. Fujishima and K. Nakata, *J. Phys. Chem. C*, **2017**, 121, 19836−19848.
22. M. Sachs, J.-S. Park, E. Pastor, A. Kafizas, A. A. Wilson, L. Francàs, S. Gul, M.

Ling, C. Blackman, J. Yano, A. Walsh and J. R. Durrant, *Chem. Sci.*, **2019**, 10, 5667−5677.

23. F. Urbach, *Phys. Rev.*, **1953**, 92, 1324.
24. S. Laursen and S. Linic, *J. Phys. Chem. C*, **2009**, 113, 6689−6693.
25. P. Schlexer, A. Ruiz Puigdollers and G. Pacchioni, *Phys. Chem. Chem. Phys.*, **2015**, 17, 22342−22360.
26. J. Xue, O. Elbanna, S. Kim, M. Fujitsuka and T. Majima, *Chem. Commun.*, **2018**, 54, 6052−6055.
27. C.-C. Nguyen, M. Sakar, M.-H. Vu and T.-O. Do, *Ind. Eng. Chem. Res.*, **2019**, 58, 3698− 3706.
28. L. Guo, Z. Yang, K. Marcus, Z. Li, B. Luo, L. Zhou, X. Wang, Y. Du and Y. Yang, *Energy Environ. Sci.*, **2018**, 11, 106−114.
29. M. Zhu, S. Kim, L. Mao, M. Fujitsuka, J. Zhang, X. Wang and T. Majima, *J. Am. Chem. Soc.*, **2017**, 139, 13234−13242.
30. K. Chang, M. Li, T. Wang, S. Ouyang, P. Li, L. Liu and J. Ye, *Adv. Energy Mater.*, **2015**, 5, 1402279.
31. K.-i. Yamanaka, T. Ohwaki and T. Morikawa, *J. Phys. Chem. C*, **2013**, 117, 16448−16456.
32. C. C. Milleville, K. E. Pelcher, M. Y. Sfeir, S. Banerjee and D. F. Watson, *J. Phys. Chem. C*, **2016**, 120, 5221−5232.
33. S. Kaniyankandy, S. N. Kaniyankandy, S. Rawalekar and H. N. Ghosh, *J. Phys. Chem. C*, **2011**, 115, 19110−19116.
34. R. Aepuru, S. Aepuru, N. Ghorai, V. Kumar, H. S. Panda and H. N. Ghosh, *J. Phys. Chem. C*, **2018**, 122, 27273−27283.
35. R. Godin, Y. Wang, M. A. Zwijnenburg, J. Tang and J. R. Durrant, *J. Am. Chem. Soc.*, **2017**, 139, 5216−5224.
36. K.-i. Yamanaka, S. Sato, M. Iwaki, T. Kajino and T. Morikawa, *J. Phys. Chem. C*, **2011**, 115, 18348−18353.
37. Z. Zheng, T. Tachikawa and T. Majima, *J. Am. Chem. Soc.*, **2014**, 136, 6870–6873.

Chapter 4. Near Bandgap Excitation Inhibits the Interfacial Electron Transfer of Semiconductor/Cocatalyst

1. Introduction

Employing semiconductor photocatalysts to promote H_2 production from water driven by solar light has attracted extensive research interest due to its potential for developing a green and sustainable energy economy.[1] Loading reduction cocatalysts onto semiconductor photocatalysts is a commonly used strategy to improve the activity of photocatalysts because cocatalysts can facilitate the spatial separation of photogenerated electron-hole pairs and provide reactive sites with the lower activation energy for H_2 evolution.[2] ET from the semiconductor to the cocatalyst is the prerequisite to display the role of the reduction cocatalysts, which occurs on the time scale of picosecond to nanosecond.[3,4] Accordingly, understanding such ultrafast IET process is essential for establishing the structure-property relationship of semiconductor/cocatalyst system.

To this end, femtosecond TA spectroscopy (TAS), a powerful tool for tracking early charge carrier kinetics, has been successfully applied to study the interfacial charge transfer kinetics of semiconductor/cocatalyst systems such as $LaTiO_2N$/Pt (or CoO_x),[5] GaN:ZnO/$Rh_{2-y}Cr_yO_3$,[6] and Ta_3N_5/Rh.[7] In most TAS studies, the electrons in the semiconductor are induced by the above bandgap excitation, while the example of the near bandgap excitation is scarce. However, in photocatalytic reactions, the near bandgap absorption also contributes to the generation of electrons, especially for semiconductors whose absorption edge is near 420 nm (e.g., CN nanosheets) given that the radiation energy of solar spectrum is mainly distributed in the $\lambda > 420$ nm (visible−NIR) region.[1] Unfortunately, there is, to the best of our knowledge, only one literature reporting the interfacial hole transfer kinetics of the semiconductor/cocatalyst system for the near bandgap excitation.[8] Not enough information of the IET kinetics has become a bottleneck for understanding the photocatalytic mechanism for H_2

evolution of the semiconductor/cocatalyst system in its entire light absorption range.

For opaque powders, the TA spectra can be obtained by collecting and analyzing the diffuse reflected light from the sample.[3,8] In this chapter, we employ the fs-TDRS to investigate the IET kinetics of a semiconductor/cocatalyst prototype, CN/Pt. We determine the IET rate and efficiency for both above and near bandgap excitations. The results show that the near bandgap excitation of CN inhibits the IET of CN/Pt due to electron deep trapping, leading to a markedly low AQE for photocatalytic H_2 evolution.

2. Experimental Section

Preparation of CN nanosheets. CN was synthesized as in Chapter 3 except that (i) urea was used as the precursor and (ii) the exfoliation time was 2 h.

Preparation of CN/Pt. CN/Pt was synthesized by an in situ photodeposition method. Typically, 40 mg of CN was dissolved into a mixture of de-ionized (DI) water (8 mL) and TEOA (2 mL). Then, 3.2 mL of 1 mg mL^{-1} $H_2PtCl_6 \cdot 6H_2O$ water solution was added into the mixture. The solution was irradiated under a UV-LED source (Asahi Spectra, POT-365, 100 mW cm^{-2}) after the deaeration with argon for 1 h. The product was centrifuged, washed, and dried under 60 °C. Herein, the theoretical weight percent of the loaded Pt is 3%.

Characterization. The samples were characterized by TEM and UV−vis DRS as in Chapter 1.

Apparent quantum efficiency (AQE) determination. The AQE for photocatalytic H_2 evolution was determined by the same method as in Chapter 2 except that the weight of the sample was 5 mg.

DFT calculation. All calculations were carried out as in Chapter 3.

Fs-TDRS measurement. The fs-TDRS were measured as in Chapter 3 except that the pump powers of 5 and 6 μJ per pulse were used for the 380 and 430 nm pumps, respectively.

3. Results and Discussion

Upon loading Pt by photodeposition, the TEM image (Figure 1) clearly shows that the ~5−10 nm-sized Pt particles are well-dispersed on CN with a lattice spacing of 0.224 nm, corresponding to the (111) crystal plane of the metallic Pt.[9] Figure 2 shows the UV−vis DRS of CN and CN/Pt. As seen, the absorption edge of CN locates at ~430 nm, corresponding to a bandgap of ~2.88 eV. After loading Pt nanoparticles, the absorption edge shows no noticeable shift. However, an obvious absorption enhancement is observed in the visible-light region, which can be attributed to the light scattering by the Pt particles.[10]

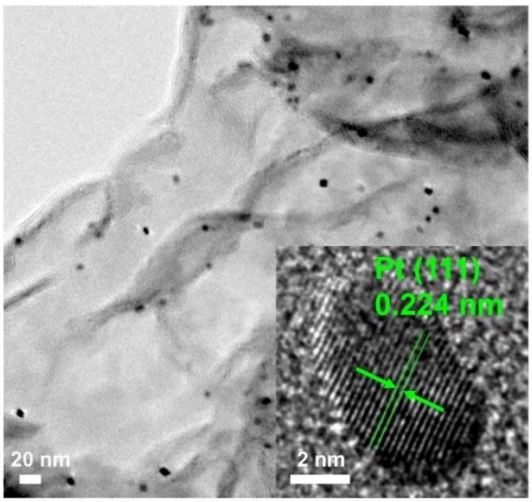

Figure 1. TEM image of CN/Pt.

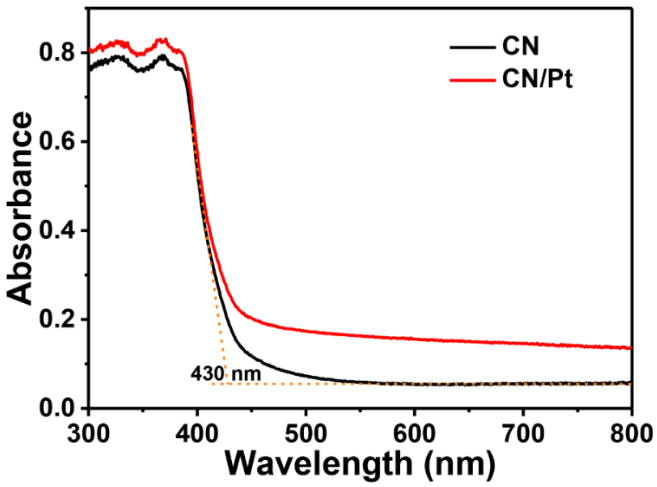

Figure 2. UV−vis DRS of CN and CN/Pt.

Following the successful synthesis of CN/Pt photocatalysts, we determined the wavelength-dependent AQEs for photocatalytic H_2 evolution over CN/Pt. Without Pt loading, CN shows no measurable activity under the monochromatic light irradiation. On the other hand, Pt acts as the cocatalyst and is inactive itself. Therefore, the observed activity of CN/Pt in Figure 3 is attributed to the ET from CN to the reactive site, Pt. In other words, the AQEs at different wavelengths depend on not only the absorption capabilities of CN, but also the ET kinetics at the CN/Pt interface. However, the latter is usually ignored in the literatures. If the latter could be ignored, the IET kinetics of CN/Pt does not vary with the wavelength, and the AQEs as a function of the wavelengths should well match the absorption spectrum of CN theoretically. However, the AQEs become markedly lower compared with the absorption spectrum at wavelengths corresponding to the near bandgap excitations (Figure 3). Such phenomenon can also be found in other systems such as CdS/Mo_2C[11] and $Bi_{12}O_{17}Cl_2/MoS_2$,[12] in which no explanation is given though. These results thereby highlight the critical role of the IET in determining the wavelength-dependent activity of semiconductor/cocatalyst for photocatalytic H_2 evolution. In the following, we interrogate the IET kinetics of the CN/Pt system by means of fs-TDRS.

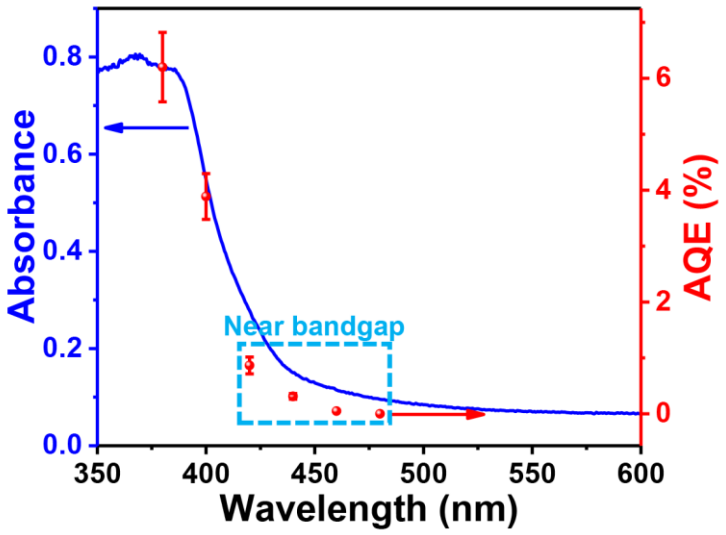

Figure 3. UV−vis DRS of CN and wavelength-dependent AQEs for H_2 evolution over CN/Pt.

In our fs-TDRS measurements, we deliberately chose to use 380 and 430 nm pump

lasers to induce the above and near bandgap excitations of CN, respectively. Meanwhile a white-light continuum probe (820−1180 nm) was employed to monitor the excited electron kinetics (free or shallowly trapped electrons).[13,14] Figure 4 shows the as-obtained TA spectra of CN and CN/Pt. It should be noted here that the contribution of Pt nanoparticles to the TA signal intensity can be ignored based on the following two points: (i) the lifetime of the hot electrons generated by exciting Pt is ultrashort (1−100 fs),[15] and (ii) the weight percentage of Pt is only 3%. By comparing CN and CN/Pt for two different excitation wavelengths (λ_{exc} = 380 and 430 nm), it can be found that Pt deposition accelerates the decay of photogenerated electrons in CN. On the other hand, it is noteworthy that photogenerated electrons in CN decay faster for λ_{exc} = 380 nm than for λ_{exc} = 430 nm, suggesting that the electron kinetics of CN is wavelength dependent.

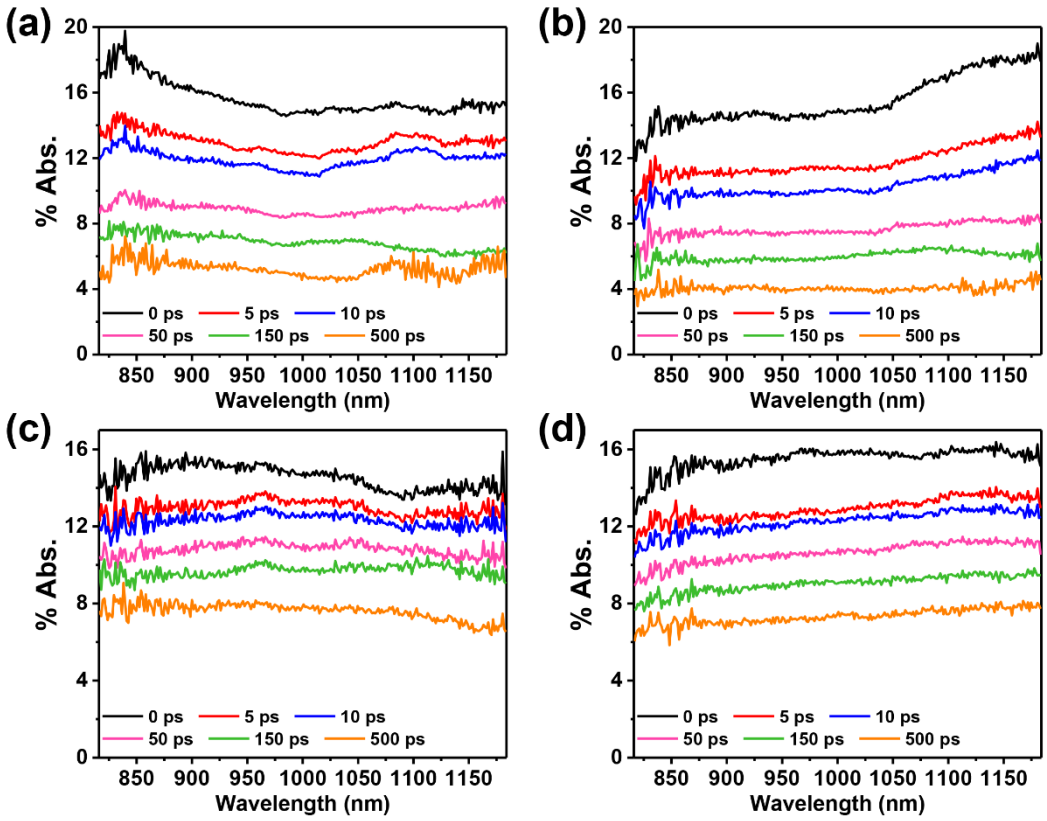

Figure 4. TA spectra of (a, c) CN and (b, d) CN/Pt upon excitations at (a, b) 380 nm and (c, d) 430 nm.

To give a clear physical picture as well as a quantitative analysis of the above results, we plot a representative set of TA kinetics probed at 950 nm in Figure 5. Like Chapter 3, the obtained kinetic parameters are given in Tables 1 and 2. In the case of bare CN,

τ_{av} (360 ps) for λ_{exc} = 430 nm is longer than that (330 ps) for λ_{exc} = 380 nm, and A_0 (0.37) for λ_{exc} = 430 nm is greater than that (0.17) for λ_{exc} = 380 nm. This indicates that λ_{exc} = 430 nm results in more electrons relaxing to deeper TSs with respect to λ_{exc} = 380 nm. Similar results were reported for $LaTiO_2N$ by Singh et al., which were explained by the time delay due to the hot electron cooling.[8] To be specific, for the above bandgap excitation, e.g., λ_{exc} = 380 nm in our case, the generated hot electrons take more time to cool down to the CB edge. Whereas, for the near bandgap excitation, no such cooling time is involved, making that electrons have more time to be trapped more deeply. However, Tamaki et al. have efficiently demonstrated that the cooling time of hot electrons are on the ultrashort time scale (sub-ps).[16] Such ultrashort delay time induced by cooling cannot explain the large lifetime difference (tens of ps) in our case. In a more general picture, the photogenerated electron with a lifetime of τ features a trapping rate constant of $k_T = 1/\tau$. Since τ_{av} for λ_{exc} = 430 nm is longer than that for λ_{exc} = 380 nm, k_T for λ_{exc} = 430 nm is smaller, indicating a lower mobility. Because the excess kinetic energy of electrons induced by the excess excitation energy for λ_{exc} = 380 nm is rapidly dissipated as heat (cooling),[17] the kinetic energy of electrons at the CB edge should be the same as that for λ_{exc} = 430 nm. Therefore, to explain the mobility difference, we propose that besides the kinetic energy, the mobility of photogenerated electrons is also influenced by the states where they locate. Our recent works have demonstrated that defects such as nitrogen vacancies intrinsically exist in CN.[18,19] DSs can overlap with the CB edge, leading to the Urbach tail absorption,[19] e.g., 430−550 nm absorption in Figure 3. For λ_{exc} = 430 nm (near bandgap excitation), the electrons are generated near the CB edge, possibly in some DSs. According to our DFT calculation results (Figure 6), the dispersion degree of defect band is lower than that of the CB edge, indicating high effective mass and limited mobility, and thereby resulting in slow k_T. In contrast, for λ_{exc} = 380 nm (above bandgap excitation), electrons cool down to the CB edge, possessing high mobility and thereby leading to fast k_T.

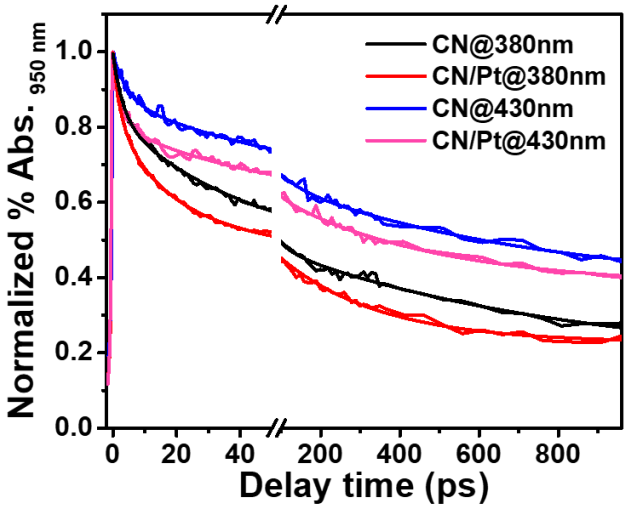

Figure 5. Normalized TA traces of CN and CN/Pt.

Table 1. Weighted coefficients of the TA Decay.

Sample[a]	A_0	A_1	A_2	A_3
CN (380 nm)	0.17	0.17	0.32	0.34
CN/Pt (380 nm)	0.23	0.16	0.27	0.33
CN (430 nm)	0.37	0.12	0.19	0.31
CN/Pt (430 nm)	0.38	0.17	0.14	0.29

Table 2. Lifetimes of the TA Decay.

Sample[a]	τ_0 **(ns)**	τ_1 **(ps)**	τ_2 **(ps)**	τ_3 **(ps)**	τ_{av} **(ps)**[b]	k_{av} **(10^9 s^{-1})**[c]
CN (380 nm)	≫1	3.1	39	760	330	
CN/Pt (380 nm)	≫1	2.2	15	250	110	6.1
CN (430 nm)	≫1	4.5	56	680	360	
CN/Pt (430 nm)	≫1	2.9	39	410	210	2.0

[a]The numbers in parentheses are excitation wavelengths. [b]Average lifetime, $\tau_{av} = \sum_i A_i\tau_i / \sum_i A_i$.

[c]Average IET rate constant, $k_{av} = 1/\tau_{av}$ (CN/Pt) − $1/\tau_{av}$ (CN).

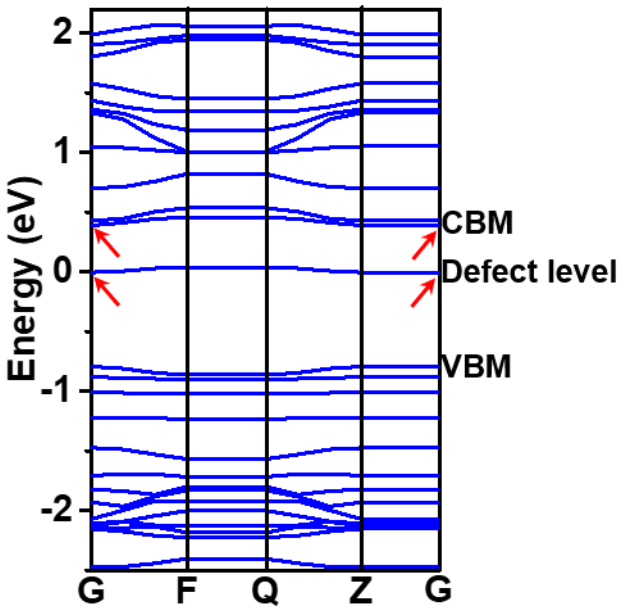

Figure 6. Calculated band structure of CN-V_n.

On the other hand, Pt loading makes τ_{av} of electrons in CN shorter (from 330 to 110 ps for λ_{exc} = 380 nm and from 360 to 210 ps for λ_{exc} = 430 nm). The lifetime decrease should be attributed to the opening of additional ET channels from CN to Pt, as in Chapter 3. The average IET rate constant, k_{av} of 2.0×10^9 s^{-1} for λ_{exc} = 430 nm is smaller than 6.1×10^9 s^{-1} for λ_{exc} = 380 nm, indicating an inefficient ET, which can be attributed to the electron deep trapping according to the model proposed in Chapter 3 (Figure 7).

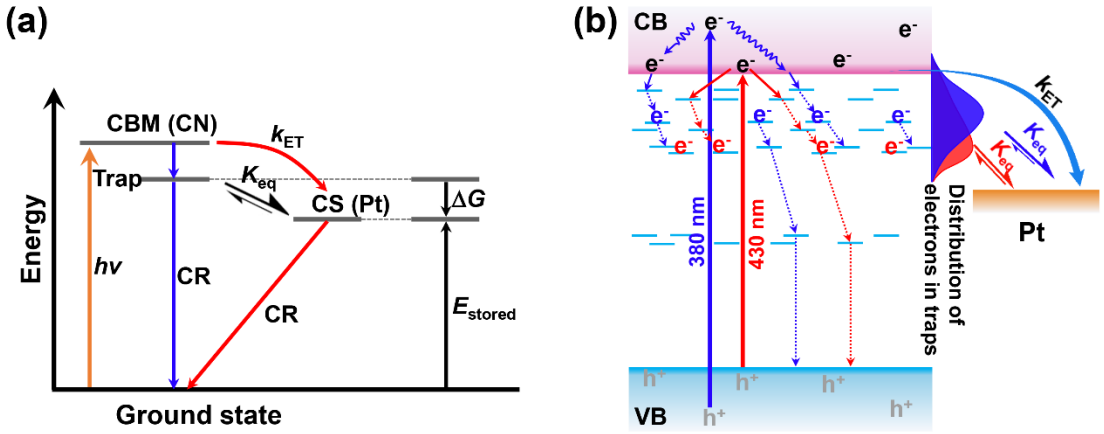

Figure 7. Schematic illustrations of (a) proposed ET model and (b) IET kinetics of CN/Pt for above and near bandgap excitations.

4. Conclusion

In summary, by the aid of fs-TDRS, we have investigated the IET kinetics of a typical

semiconductor/cocatalyst system, CN/Pt. The results show that for the near bandgap excitation (λ_{exc} = 430 nm), more photogenerated electrons relax to deeper TSs than for the above bandgap excitation (λ_{exc} = 380 nm) due to the lower mobility induced by intrinsic DSs. Such relaxation to the deeper TSs inhibits the IET, resulting in the markedly decreased AQE for photocatalytic H_2 evolution. This should be taken into consideration in the development of efficient semiconductor/cocatalyst system; the inhibited IET can be improved by the engineering of TSs as demonstrated in Chapter 3. The above findings provide kinetic insights into the photocatalytic mechanism of the semiconductor/cocatalyst system throughout its light absorption range.

5. References

1. Q. Wang and K. Domen, *Chem. Rev.*, **2020**, 120, 919–985.
2. J. Wang, Q. Zhou, T. Shen, X. Chen, S. Liu and Y. Zhang, *Langmuir*, **2019**, 35, 12366−12373.
3. K.-i. Yamanaka, T. Ohwaki and T. Morikawa, *J. Phys. Chem. C*, **2013**, 117, 16448−16456.
4. R. Godin, Y. Wang, M. A. Zwijnenburg, J. Tang and J. R. Durrant, *J. Am. Chem. Soc.*, **2017**, 139, 5216−5224.
5. A. Yamakata, M. Kawaguchi, N. Nishimura, T. Minegishi, J. Kubota and K. Domen, *J. Phys. Chem. C*, **2014**, 118, 23897−23906.
6. R. Godin, T. Hisatomi, K. Domen and J. R. Durrant, *Chem. Sci.*, **2018**, 9, 7546−7555.
7. D. H. K. Murthy, H. Matsuzaki, Z. Wang, Y. Suzuki, T. Hisatomi, K. Seki, Y. Inoue, K. Domen and A. Furube, *Chem. Sci.*, **2019**, 10, 5353−5362.
8. R. B. Singh, H. Matsuzaki, Y. Suzuki, K. Seki, T. Minegishi, T. Hisatomi, K. Domen and A. Furube, *J. Am. Chem. Soc.*, **2014**, 136, 17324−17331.
9. J. Xue, S. Ma, Y. Zhou, Z. Zhang and M. He, *ACS Appl. Mater. Interfaces*, **2015**, 7, 9630−9637.
10. Y. Shiraishi, Y. Kofuji, S. Kanazawa, H. Sakamoto, S. Ichikawa, S. Tanaka and T.

Hirai, *Chem. Commun.*, **2014**, 50, 15255−15258.

11. D. Ruan, M. Fujitsuka and T. Majima, *Appl. Catal., B*, **2020**, 118541.
12. J. Li, G. Zhan, Y. Yu and L. Zhang, *Nat. Commun.*, **2016**, 7, 11480.
13. M. Zhu, S. Kim, L. Mao, M. Fujitsuka, J. Zhang, X. Wang and T. Majima, *J. Am. Chem. Soc.*, **2017**, 139, 13234−13242.
14. M. Zhu, Z. Sun, M. Fujitsuka and T. Majima, *Angew. Chem., Int. Ed.*, **2018**, 57, 2160−2164.
15. S. Wang, Y. Gao, S. Miao, T. Liu, L. Mu, R. Li, F. Fan and C. Li, *J. Am. Chem. Soc.*, **2017**, 139, 11771–11778.
16. Y. Tamaki, K. Hara, R. Katoh, M. Tachiya and A. Furube, *J. Phys. Chem. C*, **2009**, 113, 11741−11746.
17. G. Cooper, J. A. Turner, B. A. Parkinson and A. J. Nozik, *J. Appl. Phys.*, **1983**, 54, 6463−6473.
18. J. Xue, M. Fujitsuka and T. Majima, *Phys. Chem. Chem. Phys.*, **2019**, 21, 2318−2324.
19. J. Xue, M. Fujitsuka and T. Majima, *ACS Appl. Mater. Interfaces*, **2019**, 11, 40860−40867.

Chapter 5. Shallow Trap State-Enhanced Photocatalytic Hydrogen Evolution over Thermal-Decomposed Polymeric Carbon Nitride

1. Introduction

CN is usually synthesized by a thermal polymerization method, in which the temperature plays a crucial role in determining the final structure. It is well accepted that the typical graphitic structure of CN forms at 500−600 °C, while further increasing the temperature, for example, to 660 °C results in the generation of thermal-decomposed CN,[1−3] herein denoted TCN. Despite the great research interest in the synthesis and application of CN, there remains the need to investigate the photogenerated electron kinetics that influences the H_2 evolution activity. In this regard, Durrant et al. recently studied the photogenerated electron kinetics of CN by using the time-resolved TA spectroscopy.[4] They found that electron deep trapping reduced the efficiency of photocatalytic H_2 evolution, and CN synthesized at 600 °C had the least DTSs to show the higher activity than those synthesized at 500 and 550 °C. TSs in CN are generally a result of structural defects such as N/C vacancies and $-NH_x$ terminal groups.[4,5] However, the photogenerated electron kinetics of CN synthesized at a higher temperature, namely TCN, has not been reported to date, which has prevented us from drawing an entire photocatalytic picture of CN.

In this chapter, we report, for the first time, the photogenerated electron kinetics of TCN synthesized in air by using fs-TDRS. Combined with ordinary characterizations, we find that the OFGs in TCN can modify the electronic structure of CN to introduce STSs for photogenerated electrons, leading to an efficient H_2 evolution.

2. Experimental Section

Preparation of CN and TCN. CN and TCN were synthesized by directly polymerizing

thiourea at 550 and 660 °C in air, respectively.[1] In detail, thiourea (6g) was placed in a covered crucible and heated to 550 or 660 °C in a muffle furnace for 4 h using a heating rate of 2 °C min^{-1}. Then, the agglomerates were grounded into powder.

Characterization. The samples were characterized using XRD, TEM, XPS, UV−vis DRS, and FTIR spectroscopy as in the above chapters.

Photocatalytic H_2 evolution. The photocatalytic H_2 evolution reaction was carried out like Chapter 2 except that the weight of the sample was 5 mg.

Fs-TDRS. The fs-TDRS were measured as in Chapter 3 except that the pump power of 1.9 μJ per pulse was used for the 420 nm pump.

3. Results and Discussion

Figure 1 shows the TEM images of the as-obtained samples. As shown in Figure 1a, CN mainly consists of large particles with a typical bulk morphology. In contrast, TCN displays much smaller sizes with a nanosheet-like structure due to the thermal decomposition (Figures 1b−d).

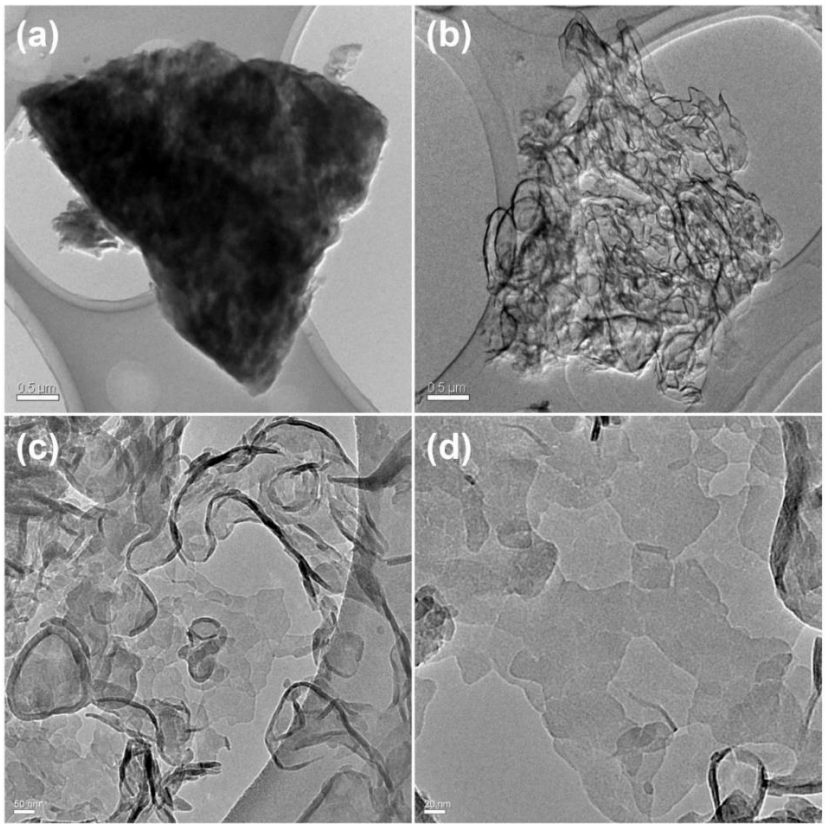

Figure 1. TEM images of (a) CN and (b−d) TCN.

The XRD patterns of CN and TCN are given in Figure 2a. For CN, two typical peaks are observed at 13.0 and 27.4°, corresponding to the in-plane repetition of the tri-*s*-triazine units (100) and the interlayer stacking of the aromatic segments (002), respectively.[6] The former peak becomes weaker for TCN, suggesting the destruction of the ordered tri-*s*-triazine units at a high temperature.[7] Meanwhile, the latter peak shifts to 27.9°, indicating a decrease of the interlayer distance.[7] To examine the bonding structure of CN and TCN, FTIR spectroscopy was performed. As shown in Figure 2b, the peaks at 3000−3500, 1230−1650, and 805 cm^{-1} are assigned to the N–H_x (x = 1 or 2)/O–H stretching, CN heterocycles stretching, and triazine unit breathing modes, respectively.[8] As compared to CN, TCN shows two new peaks at 1205 and 1670 cm^{-1}, which are assignable to C–O[9] and C=O[10] stretching modes, respectively. In addition, several small peaks at 1276, 1333, and 1430 cm^{-1} indicate that high temperature breaks the CN heterocycles. The existence of those OFGs can be further confirmed by the XPS. As shown in the C 1s spectra (Figure 2c), in addition to the two characteristic peaks of N–C=N (287.8 eV) and adventitious hydrocarbons (C–C/C=C, 284.8 eV),[11,12] two extra peaks attributed to O–C=O and C–O are observed for TCN at 289.0 and 286.4 eV,[13,14] respectively. Moreover, the possibility that TCN has more nitrogen vacancies than CN can be ruled out since no lower energy shift of the N–C=N peak is observed for TCN.[5,12] The N 1s spectra (Figure 2d) are fitted with four components including C–N=C (N_{2C}, 398.1 eV), N–$(C)_3$ (N_{3C}, 399.1 eV), C–N–H_x (400.5 eV), and charging effects (404.0 eV).[11,12] It is found that the ratio of N_{2C} to N_{3C} for TCN (2.0) is smaller than that for CN (3.2) and the N/C atomic ratio for TCN is also smaller as determined by the EA (Table 1). Such a loss of the N_{2C} atoms indicates that some N_{2C} atoms are substituted by oxygen atoms to generate C–O groups in the CN heterocycle of TCN. Besides, the smaller H/C atomic ratio also demonstrates the loss of terminal N–H_x groups for TCN (Table 1). Therefore, we propose that the terminal C–N–H_x could be oxidized to C=O groups by air at high temperature.

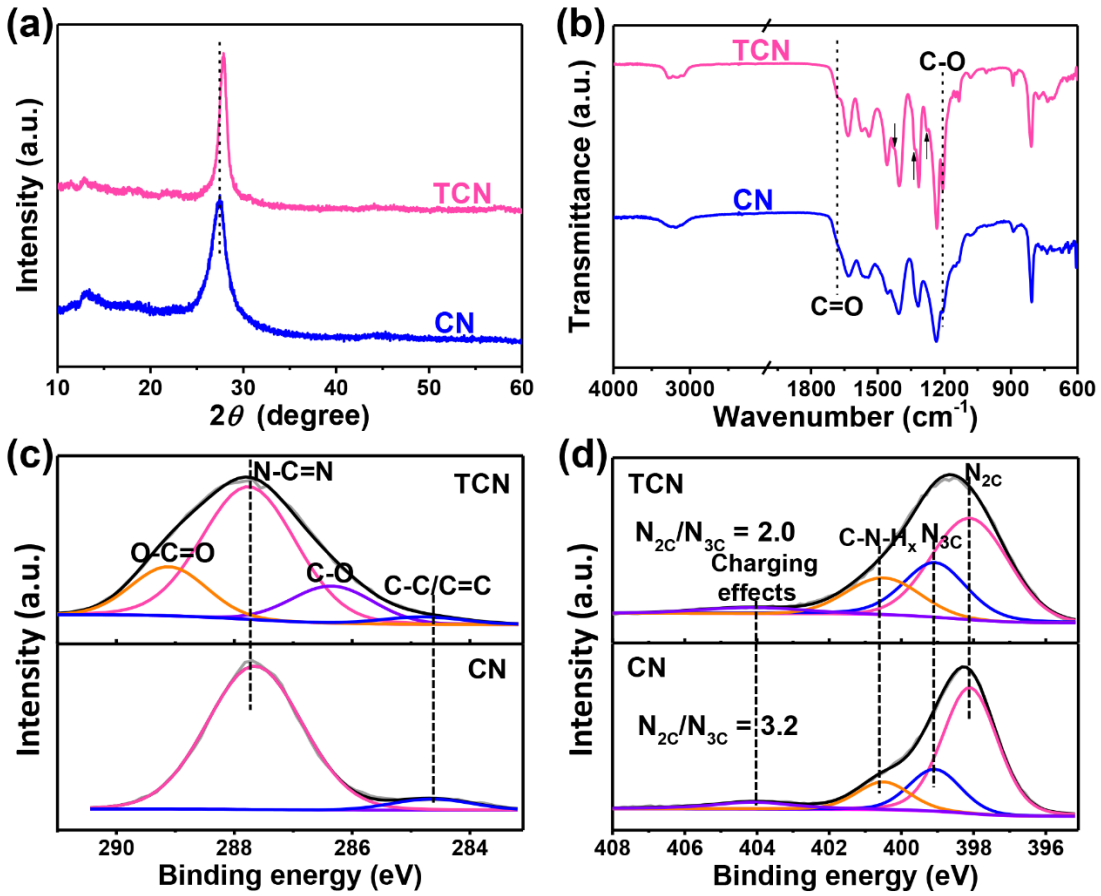

Figure 2. (a) XRD patterns, (b) FTIR spectra, (c) C 1s XPS spectra, and (d) N 1s XPS spectra of CN and TCN. The small arrows in (b) indicate the peaks at 1276, 1333, and 1430 cm^{-1}.

Table 1. N/C atomic ratios of CN and TCN determined by EA.

Sample	N (wt.%)	C (wt.%)	H (wt.%)	N/C (at.)	H/C(at.)
CN	60.18	34.06	1.96	1.51	0.69
TCN	59.10	34.67	1.72	1.46	0.60

The chemical structure difference suggests an electronic structure difference between CN and TCN. To clarify this point, UV−vis DRS combined with VB XPS were carried out. As shown by the UV−vis DRS spectra (Figure 3a), CN has an intrinsic absorption edge at ~470 nm with an add-on shoulder known as the Urbach tail that further extends the absorption to ~600 nm.[15] The tail absorption usually arises from the intrinsic defects (ID) such as N deficiencies which produce mid-gap states overlapping with the CB.[5,11] Such mid-gap states, also known as CB tail states, are hybridized from the C and N 2p

orbitals according to our previous DFT calculations.[5] Similar absorption characteristics are also observed for TCN where the absorption edge shows a blue shift due to the quantum confinement effect.[16] According to Figure 3b, the intrinsic and sub- bandgaps for CN are estimated to be 2.73 and 2.21 eV, respectively, while those for TCN are 2.95 and 2.24 eV. Figure 3c shows the VB XPS spectra of CN and TCN. The VB edges of CN and TCN occur at 1.98 and 1.74 eV below the E_F, respectively, without any VB tail states. Moreover, given that (i) the quantum confinement effect leads to the downshift of the VB,[16] and (ii) the defect states have no influence on the VB,[17] the upshift of the VB for TCN should be attributed to the newly generated OFGs.[18,19] Taken together, a schematic illustration of the electronic structures of CN and TCN can be obtained as in Figure 3d. An interesting note is that the width of the CB tail states for TCN is larger than that for CN. This suggests that other mid-gap states, possibly the OFG states (OFGSs) composed of O, C, and N 2p orbitals also exist to mix with the ID states (IDSs), resulting in the extension of the tail states. This point can be further supported by the previous report on the oxidized CN where the OFGSs are also evidenced.[19]

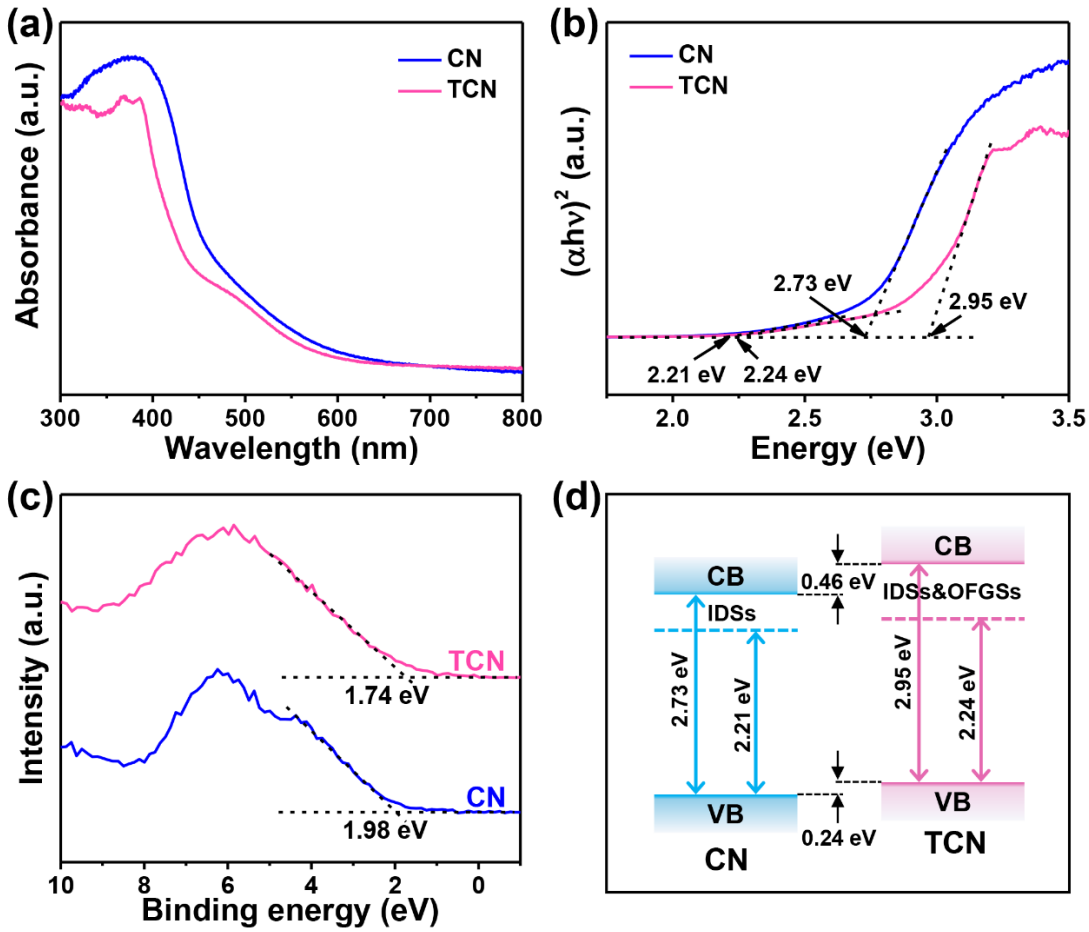

Figure 3. (a) UV−vis DRS, (b) Tauc plots for the bandgap determination, (c) VB XPS spectra, and (d) a schematic illustration of the electronic structures of CN and TCN. The blue and pink dash lines indicate the edge of CB tail states.

Upon understanding the electronic structure of CN and TCN, we are now in a position to evaluate their photocatalytic performance for H_2 evolution under visible-light ($\lambda > 420$ nm) irradiation. As shown in Figure 4a, although TCN absorbs much less visible light than CN does, the H_2 evolution rate over it is 3.2 μmol h^{-1}, which is 4 times that over CN (0.8μmol h^{-1}). Their activity under longer wavelength-light ($\lambda > 480$ nm) irradiation was also detected (Figure 4b). The results show that the H_2 evolution rate over TCN is still 1.0 μmol h^{-1}, which is 5 times that over CN (0.2 μmol h^{-1}). Thus, TCN has more advantages in the longer wavelength-light-driven photocatalysis, which is strongly related to the delocalized characteristic of OFGSs to allow electron transport. To decode the origin of the enhanced photocatalytic activity of TCN, control experiments were also performed, where no Pt cocatalyst was introduced. It was found

that neither CN nor TCN showed the activity due to a lack of active sites. Therefore, the enhanced activity of TCN is attributed to the efficient ET from TCN to Pt induced by the OFGs, considering that the amount of Pt on TCN and CN is equivalent. To provide direct evidence for it, we studied the photogenerated electron kinetics by fs-TDRS.

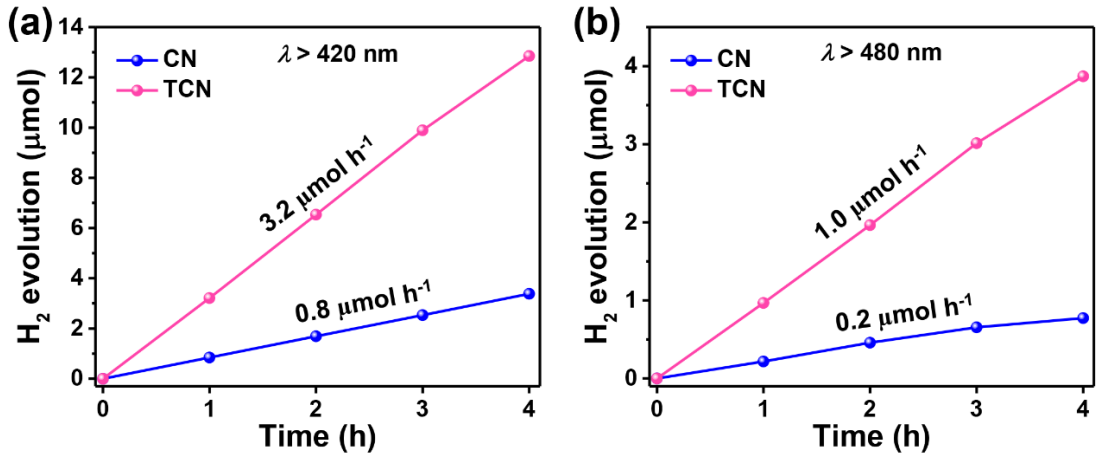

Figure 4. Photocatalytic H_2 evolution over CN and TCN under light with (a) $\lambda > 420$ nm and (b) $\lambda > 480$ nm irradiation.

The as-obtained TA spectra recorded at select time delays are given in Figures 5a and b. As seen, the TA signal of TCN decays faster than that of CN, indicating an accelerated electron decay kinetics. To draw a clear picture of the electron decay process, we report a representative set of TA traces monitored at 950 nm in Figure 5c. It is found that τ_1 and τ_2 for TCN are shorter and the corresponding weighted percentages are greater than those for CN. This indicates that TCN has more STSs compared to CN. Combined with the results from Figure 3d, it is reasonable to conclude that OFGSs can act as STSs for photogenerated electrons. According to the conclusion of Chapter 3, STSs can facilitate the IET of TCN/Pt (Figure 5d), leading to the enhanced activity for photocatalytic H_2 evolution.

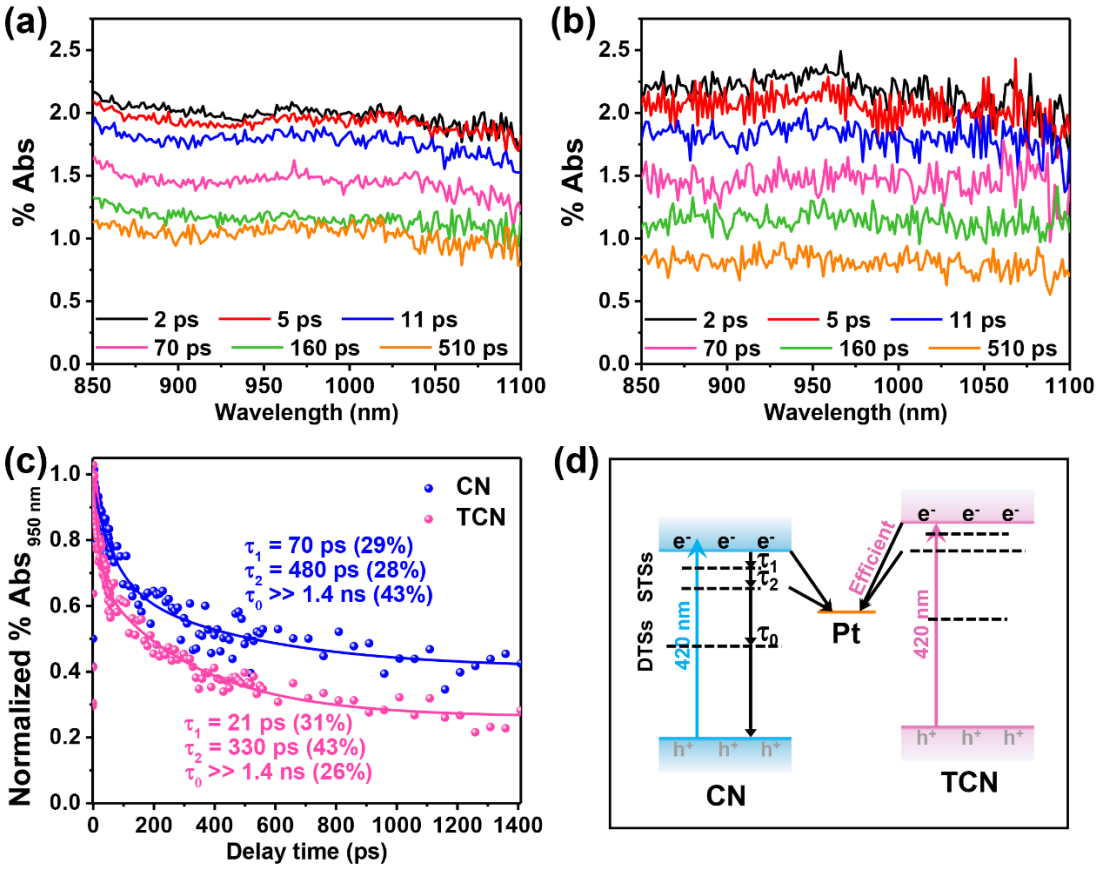

Figure 5. TA spectra recorded at select time delays of (a) CN and (b) TCN. (c) Normalized TA traces monitored at 950 nm during 420 nm laser flash photolysis, and (d) photogenerated electron kinetics of CN and TCN. The longer dash lines represent the more TSs.

4. Conclusion

In summary, we have employed fs-TDRS to investigate the photogenerated electron kinetics of TCN synthesized in air. The results show that high temperature polymerization results in the generation of OFGs in the framework of CN. OFGs add extra CB tail states as STSs for photogenerated electrons to enhance the photocatalytic activity for H_2 evolution. The above findings not only complement the kinetic understanding of the photocatalytic mechanism of CN, but also suggest that controlling the distribution of TSs, possibly through engineering the functional groups, is a promising way to further improve the activity of CN.

5. References

1. G. Zhang, J. Zhang, M. Zhang and X. Wang, *J. Mater. Chem.*, **2012**, 22, 8083–8091.
2. H. Zhang and A. Yu, *J. Phys. Chem. C*, **2014**, 118, 11628–11635.
3. H. Wang, W. Zhou, P. Li, X. Tan, Y. Liu, W. Hu, J. Ye and T. Yu, *J. Phys. Chem. C*, **2018**, 122, 17261–17267.
4. R. Godin, Y. Wang, M. A. Zwijnenburg, J. Tang and J. R. Durrant, *J. Am. Chem. Soc.*, **2017**, 139, 5216–5224.
5. J. Xue, M. Fujitsuka and T. Majima, *ACS Appl. Mater. Interfaces*, **2019**, 11, 40860–40867.
6. X. Wang, K. Maeda, A. Thomas, K. Takanabe, G. Xin, J. M. Carlsson, K. Domen and M. Antonietti, *Nat. Mater.*, **2009**, 8, 76–80.
7. P. Niu, G. Liu and H. M. Cheng, *J. Phys. Chem. C*, **2012**, 116, 11013–11018.
8. J. Zhang, M. Zhang, G. Zhang and X. Wang, *ACS Catal.*, **2012**, 2, 940–948.
9. N. Sun, Y. Liang, X. Ma and F. Chen, *Chem. – Eur. J.*, **2017**, 23, 15466–15473.
10. K. Dai, L. Lu, Q. Liu, G. Zhu, X. Wei, J. Bai, L. Xuan and H. Wang, *Dalton Trans.*, **2014**, 43, 6295–6299.
11. P. Niu, H. Li, Y. Ma and T. Zhai, *J. Phys. Chem. C*, **2018**, 122, 20717–20726.
12. J. Xue, M. Fujitsuka and T. Majima, *Phys. Chem. Chem. Phys.*, **2019**, 21, 2318–2324.
13. G. P. Lo´pez, D. G. Castner and B. D. Ratner, *Surf. Interface Anal.*, **1991**, 17, 267–272.
14. H. Wang, S. Jiang, S. Chen, D. Li, X. Zhang, W. Shao, X. Sun, J. Xie, Z. Zhao, Q. Zhang, Y. Tian and Y. Xie, *Adv. Mater.*, **2016**, 28, 6940–6945.
15. H. Yaghoubi,Z. Li, Y. Chen, H.T.Ngo,V. R.Bhethanabotla,B.Joseph, S. Ma, R. Schlaf and A. Takshi, *ACS Catal.*, **2015**, 5, 327–335.
16. G. Liu, P. Niu, C. Sun, S. C. Smith, Z. Chen, G. Q. Lu and H.-M. Cheng, *J. Am. Chem. Soc.*, **2010**, 132, 11642–11648.
17. W. Tu, Y. Xu, J. Wang, B. Zhang, T. Zhou, S. Yin, S. Wu, C. Li, Y. Huang, Y. Zhou,

Z. Zou, J. Robertson, M. Kraft and R. Xu, *ACS Sustainable Chem. Eng.*, **2017**, 5, 7260–7268.

18. F. Wei, Y. Liu, H. Zhao, X. Ren, J. Liu, T. Hasan, L. Chen, Y. Li and B.-L. Su, *Nanoscale*, **2018**, 10, 4515–4522.
19. S. Li, C. Hu, Y. Peng and Z. Chen, *RSC Adv.*, **2019**, 9, 32674–32682.

General Conclusion

In this dissertation, the defect-mediated photogenerated ET processes in a series of typical photocatalysts are studied by combining experiments and theoretical simulations. It is demonstrated that proper defects such as vacancies and OFGs can add STSs to facilitate the photogenerated ET, leading to an enhanced photocatalytic activity. However, some other kinds of defects such as cyano groups can restrict the ET by increasing the effective mass. Besides, the excitation to DSs (near bandgap excitation) also inhibits the ET due to the electron deep trapping. These negative factors should be also taken into consideration in the development of efficient photocatalysts. This study provides mechanistic insights into the defect-mediated ET, which would guide the design and optimization of ET reactions with high efficiency for photocatalysis.

List of Publications

1. **Jiawei Xue**, Ossama Elbanna, Sooyeon Kim, Mamoru Fujitsuka and Tetsuro Majima, Defect State-Induced Efficient Hot Electron Transfer in Au Nanoparticles/Reduced TiO_2 Mesocrystal Photocatalysts. *Chem. Commun.*, **2018**, 54, 6052–6055.
2. **Jiawei Xue**, Mamoru Fujitsuka and Tetsuro Majima, The Role of Nitrogen Defects in Graphitic Carbon Nitride for Visible-Light-Driven Hydrogen Evolution. *Phys. Chem. Chem. Phys.*, **2019**, 21, 2318–2324.
3. **Jiawei Xue**, Mamoru Fujitsuka and Tetsuro Majima, Shallow Trap State-Induced Efficient Electron Transfer at the Interface of Heterojunction Photocatalysts: The Crucial Role of Vacancy Defects. *ACS Appl. Mater. Interfaces*, **2019**, 11, 40860−40867.
4. **Jiawei Xue**, Mamoru Fujitsuka and Tetsuro Majima, Near Bandgap Excitation Inhibits the Interfacial Electron Transfer of Semiconductor/Cocatalyst. *ACS Appl. Mater. Interfaces*, **2020**, 12, 5920−5924.
5. **Jiawei Xue**, Mamoru Fujitsuka and Tetsuro Majima, Shallow Trap State-Enhanced Photocatalytic Hydrogen Evolution over Thermal-Decomposed Polymeric Carbon Nitride. *Chem. Commun.*, **2020**, 56, 5921−5924.

Supplementary List of Publications

1. Daming Ruan, **Jiawei Xue**, Mamoru Fujitsuka and Tetsuro Majima, Ultrafast Spectroscopic Study of Plasmon-Induced Hot Electron Transfer under NIR Excitation in Au Triangular Nanoprisms/g-C_3N_4 for Photocatalytic H_2 Production. *Chem. Commun.*, **2019**, 55, 6014−6017.
2. Zeyu Fan, Kota Nomura, Mingshan Zhu, Xinxi Li, **Jiawei Xue**, Tetsuro Majima and Yasuko Osakada, Synthesis and Photocatalytic Activity of Ultrathin Two-Dimensional Porphyrin Nanodisks via Covalent Organic Framework Exfoliation. *Commun. Chem.*, **2019**, 2, 55.

Acknowledgements

First of all, I would like to express my sincerest gratitude to Professor Mamoru Fujitsuka for his valuable supervision, guidance, and discussion throughout my doctoral study. I have learnt a lot from him, especially in the aspect of the laser flash photolysis.

I deeply appreciate Professor Tetsuro Majima for his supervision in the first half-year of my doctoral study and continuous discussions which are very helpful for my research work.

I wish to thank Associate Professor Yasuko Osakada for her kind help not only in my doctoral study but also in my daily life. Besides, I thank Associate Professor Kiyohiko Kawai for his valuable suggestions on the preparation of my doctoral defense. I also want to thank Professor Hiromi Yamashita, Assistant Professor Sooyeon Kim, Assistant Professor Yasutaka Kuwahara, and Assistant Professor Kazuo Kobayashi for their help in my experiments.

I would also like to thank the members in our research group, including Dr. Chao Lu, Dr. Ossama Elbanna, Dr. Xiaowei Shi, Dr. Aihua Yan, Dr. Jing Xu, Dr. Ke Zhang, Dr. Xiaoyan Cai, Dr. Liang Mao, Dr. Daming Ruan, Miss Jie Xu, Mr. Bo Zhuang, Miss Yue Wang, Miss Xinxi Li, Miss Shuya Fan, Mr. Zeyu Fan, Mr. Zuoyue Liu, Mr. Shunichi Miyamoto, Mr. Ryohei Suzuki, Mr. Hiroki Kawakami, Miss Haruna Kubo, Miss Arisa Tanaka, and Mr. Yuta Okada for their help in my daily life.

At last, I thank my family members for their endless supports and encouragements during my doctoral study.

XUE JIAWEI

July 2020